Photoelectrocatalysis of paracetamol on Pd–ZnO/ N-doped carbon nanofibers electrode

Amr Nada, Benjamin Orimolade, Heba El-Maghrabi, Babatunde Koiki, M. Rivallin, Maged Bekheet, Roman Viter, Daina Damberga, Geoffroy Lesage, Igor Iatsunskyi, et al.

Photoelectrocatalysis of paracetamol on Pd-ZnO/ N- doped Carbon nanofibers electrode

Amr A. Nada[a,b£]; Benjamin O. Orimolade[c£]; Heba H. El-Maghrabi[a,d]; Babatunde A. Koiki[c];

Matthieu Rivallin[a]; Maged F. Bekheet[f]; Roman Viter[g]; Daina Damberga[g]; Geoffroy Lesage[a]; Igor

Iatsunskyi[h]; Emerson Coy[h]; Marc Cretin[a]; Omotayo A. Arotiba[c,e]; Mikhael Bechelany[a*]

[a] Institut Européen des Membranes, IEM, UMR 5635, Univ Montpellier, CNRS, ENSCM, Montpellier,

France

[b] Dept. of Analysis and Evaluation, Egyptian Petroleum Research Institute, Cairo, Nasr city P.B. 11727,

Egypt.

[c] Department of Chemical Sciences, University of Johannesburg, South Africa

[d] Dept. of Refining, Egyptian Petroleum Research Institute, Cairo, Nasr city P.B. 11727, Egypt.

[e] Centre for Nanomaterials Science Research, University of Johannesburg, South Africa

[f] Fachgebiet Keramische Werkstoffe / Chair of Advanced Ceramic Materials, Institut für

Werkstoffwissenschaften und -technologien, Technische Universität Berlin, Hardenbergstraße 40, 10623

Berlin, Germany

[g] Institute of Atomic Physics and Spectroscopy, University of Latvia, 19 Raina Blvd., LV 1586 Riga,

Latvia

[h] NanoBioMedical Centre, Adam Mickiewicz University in Poznan, 3 Wszechnicy Piastowskiej str., 61-

614, Poznan, Poland

[£] Cofirst authors

* Coresponding author: mikhael.bechelany@umontpellier.fr

Abstract

The presence of pharmaceuticals in water bodies has become a major concern in recent years. An efficient and innovative way of eliminating these pollutants is through photoelectrocatalytic (PEC) degradation owing to its environmental sustainability and its ability to remove recalcitrant pollutants. In this study, palladium loaded zinc oxide/carbon nanofibers (CZnO-Pd) were employed as a novel photoanode for PEC degradation of paracetamol. The CZnO-Pd composite was prepared through electrospinning and atomic layer deposition (ALD). The obtained materials were characterized. Photoelectrochemical studies were carried out with linear sweep voltammetry and chronoamperometry. The removal efficiency was recorded using high-performance liquid chromatography coupled to a mass spectrometer detector (HPLC-MS), while the mineralization was assessed through total organic carbon (TOC) removal. The composite electrode of CZnO-Pd nanofiber showed higher photoelectrochemical activity than ZnO carbon nanofiber, which was evident in the higher photocurrent response recorded. Upon application of the material in photoelectrocatalysis, the total removal of paracetamol was achieved within 3 h with an applied current density of $10\ mAcm^{-2}$. The percentage of TOC removal was $71.20 \pm 0.31\%$ after 4 h, which indicated significant mineralization. The results obtained in the present work reveal that Pd-ZnO/C has great potential for photoelectrocatalytic removal of organic micropollutants.

Keywords: Photoelectrocatalysis; zinc oxide; carbon nanofibers; paracetamol; water treatment

1.0 Introduction

43   There is a growing need for clean and safe water for industrial and domestic use. The major threat

44   to the availability of clean water over the years is the prevalent of water pollution. Rapid

45   urbanization and industrialization contribute largely to the rise in water pollution [1–6]. Recently,

46   it has been identified that the complexity and the diversity of the nature of organic pollutants is a

47   major contributing factor to the effect of water pollution. The class of water pollutants refers to as

48   emerging contaminants that have been the focus of many research works in recent times due to the

49   recalcitrant or persistent nature and adverse effect of these pollutants [7–10]. The most common

50   examples of these emerging contaminants are pharmaceuticals. The contamination of water bodies

51   by pharmaceuticals is majorly due to improper disposal of effluents from pharmaceutical industries

52   and hospitals [11]. Additionally, effluents from households have been reported found to contain

53   pharmaceuticals due to the improper disposal of unused or expired drugs as well as human

54   excretion (urine) containing unmetabolized drugs [12,13]. Exposure to water contaminated with

55   pharmaceutical residues can result in several health problems in humans depending on the nature

56   of concentration and type of pharmaceutical as well as the duration of exposure [14]. Aquatic

57   organisms are, however, more susceptible to hazards of pharmaceutical polluted water [15,16].

58   Unfortunately, traditional/conventional water treatment methods such as filtration, coagulation

59   and adsorption have been inadequate for the complete removal of pharmaceutical pollutants from

60   water [17,18]. This has led to the development of advanced oxidation processes (AOPs). In AOPs,

61   complete mineralization of organics to carbon dioxide and water is achieved by the actions of *in*

62   *situ* generated hydroxyl radicals (strong oxidants) [19]. Common examples of AOPs for water

63   treatment are heterogenous photocatalysis, Fenton processes, ozonation and anodic oxidation

64   [18,20–22]. A recent form of AOP is photoelectrochemical oxidation (PEC). In PEC, the

65   synergistic effect of the combination of electrochemical oxidation and photocatalysis results in

66 enhanced mineralization efficiency of the AOP [23,24]. Similar to typical photocatalysis, a

67 semiconducting metal oxide is often used in PEC and irradiation of the semiconductor with the

68 light of sufficient energy results to photogeneration electron-hole pairs. The holes then react with

69 water to produce hydroxyl radicals that oxidize organic molecules. However, unlike

70 photocatalysis, the problem of rapid recombination of photogenerated electron-hole pairs is

71 reduced by the application of bias potential, which helps in driving the photogenerated electrons

72 away from the semiconducting anode [23,25–27]. Additionally, PEC offers better reusability of

73 material since the metal oxides semiconductors are used as compact and stable electrode [28].

74 Examples of commonly used metal oxides include TiO_2 [29,30], $BiVO_4$ [31], MoS_2 [32], Cu_2O

75 [33], Fe_2O_3 [34] and WO_3 [35].

76 Zinc oxide has been widely studied for its application as photocatalyst for water treatment

77 applications [36]. The wide use of ZnO can be rightly attributed to its fascinating properties such

78 as ease of synthesis, non-toxicity, abundance in nature, good photocatalytic properties, large

79 surface area, high electron mobility, remarkable thermal and chemical stability [37,38]. However,

80 due to the large band gap of ZnO (3.37 eV), it performs better with ultraviolet light irradiation. In

81 order to enhance its performance under visible light radiation, several strategies have been

82 employed, such as doping with metals, metal loading, morphological control and formation of

83 heterojunction with visible light active semiconductors [36]. ZnO nanoparticles have been

84 employed to improve the electron-mobility in perovskite solar cells [39,40]. ZnO photoanodes

85 have also found extensive applications in PEC water splitting [41–43]. Several interesting reported

86 works are also available on the use of ZnO as photoanode for PEC water treatment applications.

87 For instance, 53% removal of methylene blue dye has been recorded with the use of ZnO prepared

88 through chemical bath deposition on silicon substrates as photoanode [44]. In another study by

89   Hosseini *et al.*, enhanced PEC degradation efficiency of ZnO was achieved by doping with nickel

90   [45]. The Ni-doped ZnO achieved total removal of ciprofloxacin within 90 min with using UV

91   light irradiation when 1.87 mA cm^{-2} current density was applied. Similarly, Feng *et al.*, reported

92   87.5% PEC removal tetracycline after 3 h on Ni-doped ZnO anodes with an applied potential of

93   0.8 V [46]. The PEC performance of Ni-doped ZnO was found to be 17% higher than the undoped.

94   The increased performance of ZnO has also been reported in its heterostructures. For example,

95   100% removal of Acid Red 1 has been achieved with the use of ZnO/MoS$_2$ photoanode, which

96   was higher than 53% removal recorded on pristine ZnO anode [47]. ZnO/BiVO$_4$ photoanodes

97   have also been successfully applied for the removal of organics [48,49]. On the other hand, Carbon

98   nanofibers (CNFs) incorporating with metal oxide nanoparticles (NPs) are interesting materials

99   for water treatment via photo-electrocatalysis technique because of their high dimensional

100   stability, large specific surface, good electrical conductivity, high electrocatalytic activity as well

101   as the ability to minimize electrode surface fouling [50–52]. CNF-based electrodes are among the

102   most interesting electrode materials for water treatment [53], electrochemical water splitting

103   [54,55] and fuel cells [56]. In addition, the CNF has many active sites, good electrical conductivity,

104   mechanical stability and electrolyte diffusion [57].

105   In this present study, palladium loaded zinc oxide/carbon nanofibers are used as suitable

106   photoanode for the removal of paracetamol as a model pollutant. The composite materials were

107   prepared through the combination of atomic layer deposition and electrospinning. ZnO/CNFs

108   materials were firstly prepared through electrospinning. This is because of the advantages of

109   electrospinning, such as being a low-cost method and the ease of controlling the size, porosity and

110   morphology of nanofibers [58–60]. Moreover, carbon nanofibers have proven to possess attractive

111   attributes, including high electrical conductivity and excellent mechanical stability. ALD was

subsequently used to deposit palladium on the ZnO/CNFs because, with ALD, the nanoscale dimensions of nanoparticle thin films can easily be controlled [61–63]. The extent of PEC removal and mineralization of paracetamol molecules using the fabricated electrode was studied in detail using chromatographic technique and total organic carbon evaluation. From the results obtained, the prepared anode has great potential for the removal of organics from wastewater through PEC applications.

2. Experimental

2.1 Materials and chemicals

Polyacrylonitrile (PAN, Mwt ~150000, CAS 25014-41-9, Sigma-Aldrich), Zinc (II) acetate dihydrate (Ni(OCOCH$_3$)$_2$·2H$_2$O, 99.9%, CAS No. 5970-45-6, Sigma-Aldrich), N,N-Dimethylformamide (DMF, 98%, CAS No. 68-12-2, Sigma-Aldrich) and ethanol (C$_2$H$_5$OH, 99%, CAS No. 64-17-5, Sigma-Aldrich) were used for electrospinning of CNFs decorated with ZnO NPs. Palladium (II) hexafluoroacetylacetonate (Pd(C$_5$HF$_6$O$_2$)$_2$, CAS 64916-48-9, 99%, Sigma-Aldrich) was used as Pd precursor and formaldehyde (HCHO, CAS No. 50-00-0, 37%, Sigma-Aldrich) used as co-reactant for ALD deposition of Pd NPs. Milli-Q water was used without further purification. Paracetamol (CAS number: 103-90-2), sodium sulphate (anhydrous, ≥99%; CAS number: 7757-82-6), absolute acetone (99%; CAS number: 67-64-1), formic acid (CAS number: 64-18-6), acetonitrile (HPLC grade; CAS number: 75-05-8), isopropanol (≥99.5%; CAS number: 67-63-0), sodium ethylenediaminetetraacetate (≥98%; CAS number: 6381-92-6) and p-benzoquinone (≥98%; CAS number: 106-51-4) were obtained from Sigma-Aldrich (Germany).

2.2 Synthesis of ZnO-Carbon Nanofibers composites

Zn@CNF was prepared by electrospinning followed by thermal preoxidation and then thermal treatment (CZnO). First, 2 g PAN powder was dissolved in 20 mL DMF under vigorous magnetic stirring until obtaining a uniform PAN precursor solution. Then, 1 g zinc acetate powder was added. The mixture solution was lifted under stirring overnight to the obtained Zn- PAN precursor solution. The electrospinning process was performed at a distance of 15 cm (solution syringe tip to collector), a voltage of 15 kV, a feeding rate of 0.5 ml/min, and a drum rotation speed of 300 rpm. The as-prepared Zn-PAN nanofibers first underwent peroxidation step at 250 °C for 2 h in an air atmosphere and then a thermal carbonation step at 800 °C for 1 h in N_2 atmosphere. The heating and cooling rates were kept constant at 1 °C/min. For comparison CNFs were prepared as the previse method without Zn precursor (CNF sample).

2.2 Deposition of Pd@ ZnO-Carbon Nanofibers composites

The ALD deposition of Pd was carried out in a low-pressure thermal (home-built) ALD reactor. A detailed description of this reactor can be found in a previous study [54]. The precursors, consisting of $Pd(hfac)_2$ and reducing agent formalin, were contained in stainless steel cylinders whose lines were heated at 70 °C and 100 °C, while the deposition chamber was pre-heated at 220 °C. The ALD cycle used for this study was consisted of 5 s pulse of $Pd(hfac)_2$, 15 s exposure, and 10 s purge, while the formalin had 1 s pulse, 15 s exposure, and 60 s purge. The ALD cycles were repeated 100 and 200 times to get CZnO-Pd100 and CZnO-Pd200, respectively.

2.3 Characterisation of materials

The crystallinity of the prepared materials was analysed using X-ray diffraction (XRD) with a PANAlytical Xpert-PRO diffractometer equipped with an Xcelerator detector and using a Ni-filtered Cu-radiation (CuKα1 radiation wavelength 0.1540598 nm and CuKα2 radiation wavelength 0.1544426 nm). Raman spectra were measured on a Senterra Bruker using a doubled Nd:YAG laser (λ= 532 nm) at a power of 10 W and an objective microscope lens of 100x. The elemental composition on the surface of the grown thin films was determined by X-ray photoelectron spectroscopy (XPS) on an Escalab 250 (Thermo Fisher Scientific, USA) using a monochromatic Al K Alpha (1486.6 eV) at 2kV and 1 μA. The morphology of nanofibers was put in evidence by using a Hitachi S4800 (Japan) scanning electron microscope (SEM). The fiber morphology was also examined using high-resolution transmission electron microscopy (HRTEM, JEOL JEM 2100, Japan) working at 200kV equipped with energy-dispersive X-ray (EDX) spectroscopy. Diffuse reflectance was measured by using HR2000+ Ocean Optics spectrometer (USA), integration sphere and Deuterium-Tungsten Halogen light source DH-2000. Photoluminescence (PL) spectra of samples were measured in the range of 350-850 nm using HR2000+ Ocean Optics spectrometer (USA). Excitation of photoluminescence was performed by Nd:YAG laser (China) (λ=266 nm, output power 29 mW).

2.4 PEC degradation experiments

The prepared materials were deposited onto FTO glass with a coverage of approximately 1 cm^2 and were used as electrodes (photoanodes). The experiments were carried out in a 100 mL capacity undivided two-electrodes cell and a power source (CNB Electronique, EU) was used to control the applied current within the cell. Platinum mesh was used as the cathode and its distance from the anode was kept constant at 3 cm. A 150 W linear halogen lamp (in the range of 420-600 nm) was

178   used as the light source and the photoanode was irradiated from the rear with a distance of 20 cm

179   from the lamp. The working solution consisted of 50 mL 0.1 mM paracetamol prepared in a

180   solution of 50 mM Na_2SO_4 (supporting electrolyte). All the experiments were performed at neutral

181   pH. Sample aliquots were taken at specified time intervals (20, 40, 60, 90, 120, 150, 180 min) for

182   paracetamol concentration and total organic carbon contents.

183   **2.5 Analytical Procedures**

184   Decrease in the total organic carbon (TOC) was used to assess the extent of mineralization of the

185   paracetamol molecules by measuring the TOC contents of the initial and aliquots solutions on a

186   TOC-L CSH/CSN Shimadzu (Japan) analyzer. Calibration curves for total carbon (TC) and

187   inorganic carbon (IC) analysis were built up by automatic dilution of standards solutions of TOC

188   (potassium hydrogen phthalate) and IC (sodium hydrogen carbonate). The TOC data obtained were

189   then used to estimate the mineralization current efficiency (MCE, %) of the solutions over a

190   specified time t (h) using equation 1 [64].

191    $$MCE(\%) = \frac{nFV_s\Delta(TOC)_{exp}}{4.32\times10^7 \; mIt} \cdot 100 \qquad\qquad (1)$$

192

193   The number of electrons consumed in the mineralization of each paracetamol molecule is

194   represented by n, F is the Faraday constant (96485 C mol^{-1}), V_s is the solution volume (L),

195    $\Delta(TOC)_{exp}$ is the experimental TOC decay (mg L^{-1}), 4.32×10^7 is a conversion factor (3600 s

196   h$^{-1}\times$12000 mg carbon mol^{-1}), m is the number of carbon atoms in each paracetamol molecule (8

197   atoms), the current passing through the system in time t is denoted as I. The number of electrons

198   (n) consumed for complete mineralization was 34 for the paracetamol molecule, according to the

199   stoichiometry of the reaction in equation 2 [65]:

200 $$C_8H_9NO_2 + 14H_2O \rightarrow 8CO_2 + NH_4^+ + 33H^+ + 34e^- \qquad (2)$$
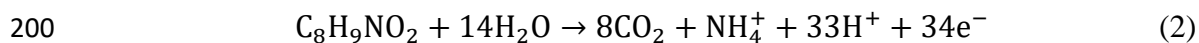
201 The concentration decay of paracetamol molecules was estimated through high performance liquid

202 chromatography – mass spectrometry (HPLC-MS). HPLC-MS was carried out with a Waters 2695

203 pump, an auto sampler with 20 μL loop, a Waters 2695 separation module (HPLC), and a Waters

204 Micromass (Wythenshawe, Manchester, UK) Quattro Micro mass spectrometer equipped with ESI

205 (Electrospray Ionization). HPLC was performed on a Waters – Xselect HSS T3 column at a column

206 temperature of 25 °C. The mobile phase was a Buffer A (HPLC grade water + 0.1% formic acid)

207 and Buffer B (HPLC grade acetonitrile + 0.05% formic acid). The flow-rate was constant at 0.25

208 mL min^{-1}, with a split of 20% to the mass spectrometer. The triple quadrupole MS was operated

209 in selected-ion-recording (SIR) mode with compounds being ionized in the negative electrospray

210 ionization mode. To achieve the best sensitivity, the MS was adjusted to facilitate the ionization

211 process. The detection conditions were: capillary potential 3.5 kV, cone potential 30 V, source

212 temperature 120 °C, desolvatation temperature 450 °C, cone gas flow 50 L h^{-1}, and desolvatation

213 gas flow 450 L h^{-1}. Nitrogen (99.5% purity) was the nebulizer gas.

214

Results and discussion

3.1 Characterisation results

217 The CNF and CZnO were elaborated via electrospinning of polymeric solution containing PAN

218 and zinc acetate as precursors, followed by pyrolysis under nitrogen at 800 °C for 1 h in N_2. CZnO-

219 Pd100 and CZnO-Pd200 samples were prepared on CZnO as a substrate by the deposition of

220 metallic Pd by ALD using 100 and 200 cycles, respectively. As shown in Figure 1a, two broad

221 reflections, which correspond to the (002) and (101) reflections of a turbostratic structure of carbon

222   [66], are observed in the XRD pattern of CNF sample. The crystallite size of the turbostratic carbon

223   along the c-axis (L_c) in CNF is found to be 0.8 nm, as revealed by Rietveld refinement of XRD

224   data. Moreover, the average number of graphite stacking layers (N_c), which is estimated from the

225   interlayer spacing d_{002} and crystallite size along the c-axis (L_c) [67], is found to be 2.5. The

226   intensities of these XRD reflections in the XRD pattern of CZnO are varnished, indicating that the

227   structure of carbon becomes highly disordered by introducing ZnO to the surface of the nanofibers.

228   Moreover, no XRD reflections corresponding to any of crystalline Zn or ZnO are observed in the

229   XRD pattern of CZnO, CZnO-Pd100 and CZnO-Pd200 samples, which can be explained by the

230   amorphous structure or small weight fractions of ZnO in these samples in order to be detected by

231   XRD measurements. However, XPS analysis (Table S1) shows that the CZnO sample contains a

232   high amount of elemental Zn (6.7 wt%, which corresponds to 8.3 wt% of ZnO) on the surface of

233   carbon nanofibers, suggesting the amorphous structure of ZnO in the sample. In contrast, Pd

234   crystallized in metallic form in CZnO-Pd100 and CZnO-Pd200 samples during ALD deposition.

235   All the peaks appearing on the XRD patterns can be indexed to the cubic structure of metallic Pd

236   (PDF No. #00-065-6174). A similar crystallite size of 3.7 nm is determined by Reitveld refinement

237   for metallic Pd in both samples, which suggests that the increase in the deposition time might

238   increase the number of deposited Pd particles on the surface of carbon nanofibers, but without

239   altering their crystallinity.

240   The incorporation and structure of ZnO and Pd on the surface of carbon nanofibers were further

241   investigated by Raman spectroscopy (Figure 1-b). All the prepared nanofibers displayed the

242   fingerprint bands of carbon, such as the disorder peak (D-band) at 1354 cm^{-1} and graphite peak

243   (G-band) at 1591 cm^{-1}. The presence of D band, which is characteristic of the disordered sp^2-

244   hybridized modes in the rings, confirms the turbostatic structure of carbon in the samples as

11

revealed by XRD. In contrast, the G-band corresponds to the vibrational stretching mode of in-plane sp2 -hybridized C atoms [68]. The relative intensities ($R = I_D/I_G$ value) of D and G bands could be used to evaluate the degree of structurally ordered graphite crystallites in carbon materials.[53] The R value of CNF was 0.93, and it increased to 1.18, 1.14 and 1.15 for CZnO, CZnO-Pd100 and CZnO-Pd200, respectively, indicating the increase in the degree of disordered carbon structures with introducing ZnO into the carbon nanofibers, which is in good agreement with XRD results. Moreover, no Raman modes were observed for ZnO in the spectra of CZnO, CZnO-Pd100 and CZnO-Pd200 samples, confirming the amorphous structure of ZnO as revealed by XRD analysis. In addition, strong bands are detected at 633 and 629 cm^{-1} in the Raman spectra of CZnO-Pd100 and CZnO-Pd200, respectively, which can be attributed to the active B_{1g} vibration modes of PdO [69]. The presence of PdO in the CZnO-Pd100 sample is also confirmed by XPS characterization, as discussed below.
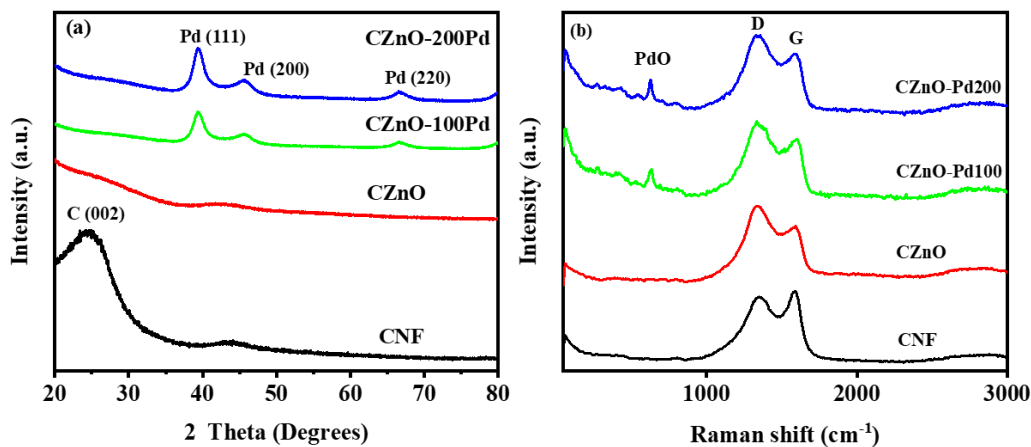
**Figure 1:** (a) XRD patterns of prepared CNF, CZnO, CZnO-Pd100, CZnO-Pd200 nanofibers. (b) Raman spectra of prepared nanofibers.

261 The elemental compositions as well as the coordination and the oxidation states of different

262 elements in the obtained samples were characterized by XPS measurements. As shown in Figure

263 S1 and Table S1, the survey XPS spectra confirm the successful incorporation of elemental Zn and

264 Pd at the surface of the carbon nanofibers. The mass fraction of elemental Zn on the surface of

265 CZnO sample is found to be 6.7 wt% and decreased to 4.1 wt% on the surface of CZnO-Pd100

266 due to the successful deposition of Pd (i.e., 33 wt% of the sample). Additionally, remarkable

267 amounts of nitrogen are detected in all the samples, suggesting the nitrogen doping of the carbon

268 nanofibers. The N-doping of carbon nanofibers can be explained by the high content of N in PAN

269 polymer and the pyrolysis of the polymeric precursors under N_2 atmosphere. As shown in Table

270 S1, the mass fraction of N in CZnO sample is four times higher than that in the CNF samples,

271 which indicates that zinc salt might stabilize the nitrile group in the polymer during the

272 electrospinning process, and thus, it enhanced the N-doping of carbon nanofibers. The high-

273 resolution XPS spectra of C 1s, O 1s, N 1s, Zn 2p, and Pd 3d orbitals are shown in Figure 2 a-e.

274 The spectrum of C 1s (Figure 2-a) could be deconvoluted into four peaks located at about 284.6,

275 285.6, 287 and 289 eV, corresponding to sp^2 hybridized graphitic carbon C-C bond, C-N bond, C-

276 O bond, and C=O bond, respectively [70]. As shown in Figure 2-b, O 1s spectrum of CNF sample

277 can be fitted with two peaks at 532.2 and 534 eV, which can be attributed to C=O and C-O bond,

278 respectively. An additional peak is observed at about 530.5 eV in the O 1s spectra of CZnO and

279 CZnO-Pd100 samples, which can be assigned to the lattice oxygen of ZnO. As displayed in Figure

280 2c, the N 1s spectra can be fitted with three peaks a ~ 398, 399.4 and 400.9 eV, which can be

281 assigned to pyridinic N, pyrrolic N and graphitic N, respectively. The pyridinic N and pyrrolic N

282 species become the dominant nitrogen species in CZnO and CZnO-Pd100 samples, suggesting the

283 improvement of the electrochemical performance of these samples [70]. The incorporation of ZnO

284   in CZnO and CZnO-Pd100 samples is further confirmed by detecting the peak at 1022 eV

285   corresponding to Zn 2p3/2 in ZnO (Figure 2d) [71]. The Pd 3d spectrum of In CZnO-Pd100

286   nanofiber (Figure 2-e) can be deconvoluted into two peaks at ~ 335.6 and 337 eV, corresponding

287   to Pd^0 and Pd^{+2} species, respectively. The Pd^{+2}/Pd^0 ratio is found to be 0.15, suggesting the small

288   mass fraction of oxidized Pd^{+2} species in the samples, which agrees with the results of Raman

289   characterizations.
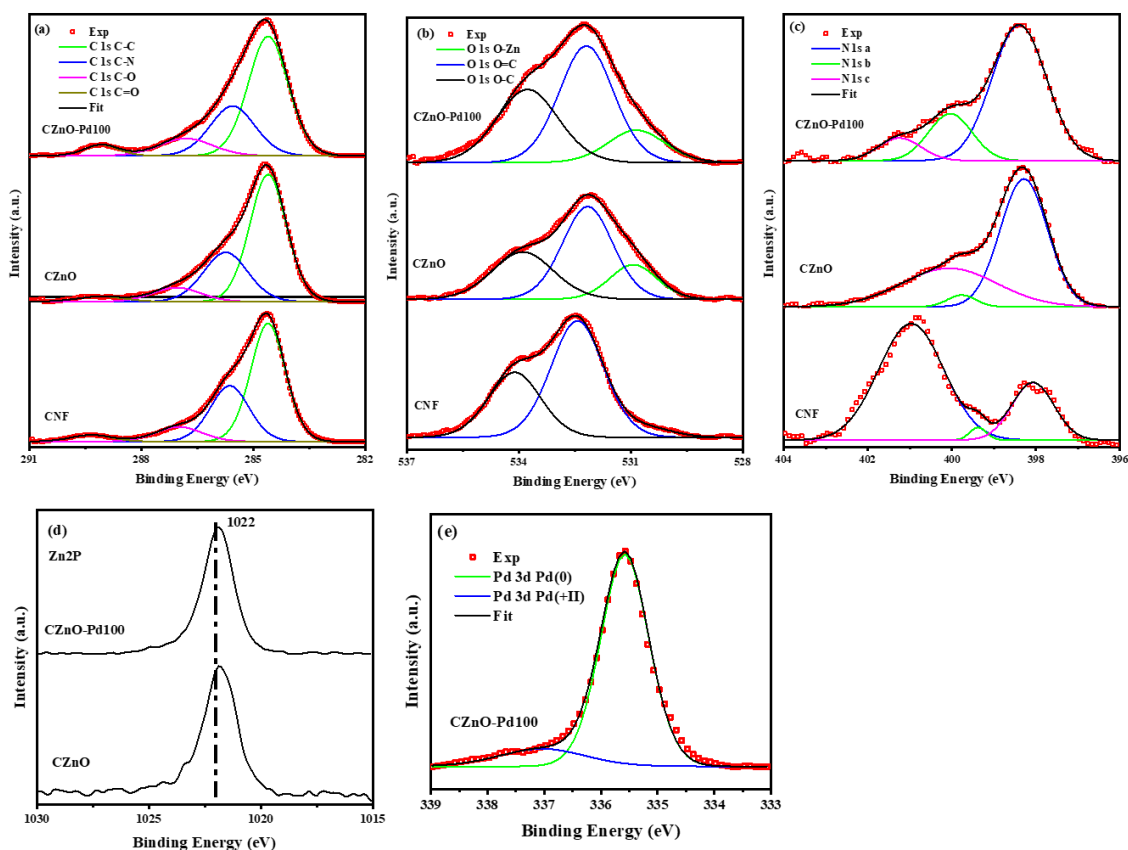
290

291   **Figure 2:** (a) High-resolution XPS spectra of C 1s (a), O 1s (b), N 1s (c), Zn 2p (d), and Pd 3d (e)

292   for CNF, CZnO and CZnO-Pd100.

293

14

294   The morphology of the elaborated nanofibers was investigated by SEM characterization, as

295   illustrated in Fig. 2(a-h). The CZnO, CZnO-Pd100 and CZnO-Pd200 samples consist of carbon

296   fibers with an average diameter of 0.25 ± 0.02 µm, which is smaller than that of CNF sample (0.45

297   ± 0.02 µm). This result suggests that the addition of zinc salt during the electrospinning process

298   hinders the growth of the carbon nanofibers during the pyrolysis. As shown in Figure 3e-h, the

299   metallic Pd are uniformly deposited as spherical particles with an average diameter of 5.6 ± 1nm on

300   the surface of the carbon nanofibers in the CZnO-Pd100 and CZnO-Pd200 samples. Although the

301   particle size of metallic Pd does not change with increasing the deposition time, the number of

302   metallic Pd increases, which agrees with XRD results. The homogeneous distribution of Zn on the

303   entire surface of carbon nanofibers is confirmed by TEM, STEM, and EDX mapping, as presented

304   in Figure S2. In contrast, the metallic Pd nanoparticles are deposited on the edge/shell of the

305   nanofibers to form coaxial or core/shell structure, as revealed by HRTEM (Figure 3i-l) and EDX

306   mapping (Figure 3m-o). The fast Fourier transform (FFT) pattern of CZnO-Pd100 nanofibers for

307   a square box (inset Fig. 3l) confirmed the cubic structure of metallic Pd nanoparticles by detecting

308   the d spacing 0.23 nm corresponding to the (111) planes of metallic Pd.

309

310
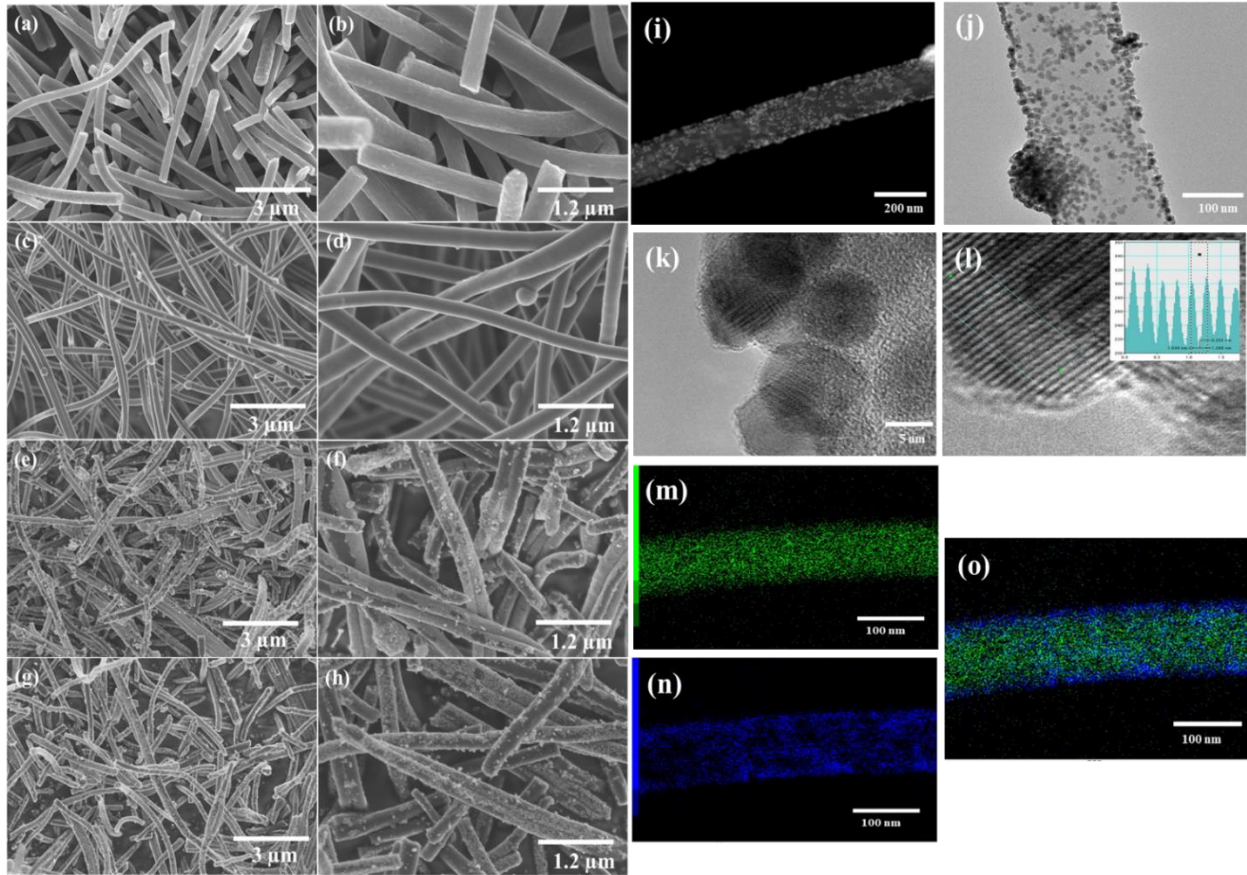
Figure 3: Field emission SEM images of the prepared nanofibers; CNF (a,b), CZnO (c,d), CZnO-

Pd100 (e,f), and CZnO-Pd200 (g,h). High-resolution transition microscope of CZnO-Pd100 (i - l)

and the fast Fourier transform (FFT) pattern of the area marked by the blue square box of CZnO-

Pd100 and the corresponding intensity profiles in inset (l), with EDX elemental mapping of CZnO-

Pd100 the zinc (m), palladium (n) and Zn overlap Pd (o).

In the next step, the optical properties influence of Pd on CZnO nanofibers were detected by the

optical band gap by UV-vis. in addition, the generation and stability of e^-/h^+ were detected by PL

side by side of determine the optical band gap. The measured reflectance spectra were converted

into absorption spectra according to equation 1 [72].

321
$$F = \frac{(1-R)^2}{2 \cdot R} \; (*) \qquad \text{equation 1}$$

322 where the parameters F and R refer to the absorption coefficient and diffuse reflectance of the

323 sample, respectively. The obtained spectra are shown in Figure 4a. All samples show low

324 absorbance in the UV range and high absorbance in the visible range. Although no absorption edge

325 is observed for ZnO-based samples, absorbance value is increased in the visible range by adding

326 ZnO and Pd on the surface of carbon nanofibers. This finding will be explained further.

327 PL spectra of the samples are shown in Figure 4b. Weak characteristic PL peak is observed at 3.25

328 eV in the spectrum of CNF sample, which could be related to delocalized π electrons available at

329 the surface of carbon nanofibers [73]. The successful addition of ZnO on the surface of carbon

330 nanofibers is confirmed by the strong PL peak at 3.24 eV observed in the spectrum of CZnO

331 sample that corresponds to ZnO excitonic emission [72]. The deposition of metallic Pd on the

332 surface of ZnO/CNF had different effects on ZnO emission: enhancement of ZnO emission in

333 ZnO-PD100 samples and quenching for ZnO-PD200 samples. According to the literature [74–78],

334 Pd nanostructures have at least 2 absorption bands: in UV and visible ranges, related to localized

335 surface plasmon resonance (SPR) effect [74–78]. The position and FWHM of the bands depend

336 on the size and shape of Pd nanostructures [79]. It was shown that due to differences between ZnO

337 and Pd work functions, Schottky barrier is expected at ZnO/Pd interface, inducing electron flow

338 from conduction band (CB) of ZnO to Pd [79,80]. It results in increase of absorption and decrease

339 of ZnO emission. However, alternative mechanisms at ZnO/Pd interface are possible [69,71]. It

340 was reported that UV emission of ZnO can be increase due to passivation of surface states during

341 Pd deposition [79,81]. We suppose, that Pd morphology will define the ZnO/Pd optical properties.

342 Comparative analysis of absorption and photoluminescence spectra points to the fact, that the

343 absence of characteristic absorption edges of ZnO in ZnO/Pd nanostructures points to hot electron

344 effect (HEE) in Pd nanoparticles [82]. This is effect is based on transition of excited SPR electrons

345 from Pd to CB of ZnO [82]. The hot electron effect is assisted with increase of visible absorption

346 and fading of UV absorption bands [82]. The HEE depends on morphology of ZnO/Pd interface.

347 At lower Pd concentrations, Pd layer is cluster-like and increase of PL can be observed. The

348 increase of Pd thickness might promote light scattering (no excitation light in absorbed by ZnO)

349 and, thus, diminishing ZnO emission.

350 Moreover, the increase in the absorbance of carbon-based samples (Figure 4a) points to a wide

351 absorbance band of Pd nanostructures in the range of 1.5-3 eV. The absorption values increase

352 with increasing the amount of Pd on the surface of carbon nanofibers. Forming of carbon-ZnO and

353 Pd/ZnO interfaces makes impact on photoluminescence properties of the composite nanomaterial

354 [81,83–85]. The presence of carbon nanofibers with ZnO results in quenching of

355 photoluminescence due to charge transfer [83]. Deposition of Pd layer over ZnO could result in

356 quenching of visible PL [81,84] and/or quenching of PL in all measured spectra due to the

357 passivation of ZnO photoluminescence centers [85]. The common effect in Pd/ZnO nanostructures

358 was observed in blue shift of UV PL peak [81,84,85]. In the present work, no shift of PL was

359 observed for ZnO/Pd100 samples. The increase of Pd concentration resulted in almost complete

360 quenching of the PL. However, the UV peak in CZnO/Pd sample was similar to the PL peak in

361 untreated CNF.

362 It was shown that UV emission in carbon nanomaterials corresponds to π- π transition in C=O

363 bonds [86,87]. The observed emission could be explained from oxidized surface of CNF in case

364 of full passivation of ZnO emission centers.

365   In addition, the valence band (VB) XPS was studied for the extra analysis of electronic states

366   induced by defects above the valence band as presented in Figure 4c-d. It is clearly seen few XPS

367   features at 2.5 eV, 5 eV and 10 eV attributed to Pd 4d, O 2p and Zn 3p peaks, respectively.

368   Typically, the density of states of ZnO below Fermi level is consisted from two bands: the upper

369   peak at ~10 eV mainly derived from Zn 3d orbitals, and the lower band at ~5 eV arises from

370   almost O 2p hybridized with the Zn 4s and Zn 4p states [88]. We estimated the VB maximum

371   (VBM) using standard method as described elsewhere [89]. The VB spectrum for the CNF is in a

372   good agreement with those reported for carbon [90]. The VBM of Pd (estimated from the

373   extrapolation) was observed at around 2 eV above the Fermi level (EF) indicating the metallic

374   behavior, while the VBM for CZnO had a value around 1.9 eV below the EF. Typically, the values

375   of VBM for undoped crystalline ZnO are in the range of 2.54 eV to 2.11 eV. This shift of the VBM

376   might be associated with an increase in the concentration of defects and/or doping (carbon,

377   nitrogen etc.) of ZnO. Besides, we may observe the shift of Zn 3p maxima from 10.19 eV to 10.42

378   eV after the Pd deposition. This can be explained by the redistribution of electron density in the d-

379   orbitals of the Zn^{2+} and the Pd^{2+} which is believed to have produced additional energy levels near

380   the VB of the ZnO narrowing its band gap, what as a consequence may change photocatalytic

381   properties of produced nanocomposites [89].

382   Hydrogen Evolution Reaction (HER) of the prepared nanofibers has been studied to manifest the

383   role of palladium. The HER linear sweep voltammetry curves (LSV) of the prepared nanofibers

384   were presented in Figure 4e. From the data, the CZnO-Pd100 has better electrochemical activity

385   than other prepared nanofibers. It was shown lower overpotential than other nanofibers (250 mV)

386   at 10 mA/cm^2 of the current density. In contrast, the overpotential of CNF, CZnO and CZnO-

387   Pd200 are 695, 620 and 441 mV at 10 mA/cm^2 of the current density, respectively. CZnO-Pd100

388   recorded the best activity of HER due to the good distribution of Pd NPs on the nanofibers. We

389   note here that the CZnO-Pd200 has less activity than CZnO-Pd100 because of the Pd NPs

390   aggregation on the surface of the nanofibers as reported elsewhere [52,54,91]. Furthermore, the

391   electrochemical impedance has been measured as illustrated in Figure 4f. The charge transfers

392   resistance (Rct) was calculated from the Nyquist plots in Figure 4f. The CZnO-Pd100 recorded

393   lower resistance (80 Ω) than the other nanofibers CNF (275 Ω), CZnO (240 Ω) and CZnO-Pd200

394   (120 Ω), in agreement with its HER activity results and lower overpotential.

395
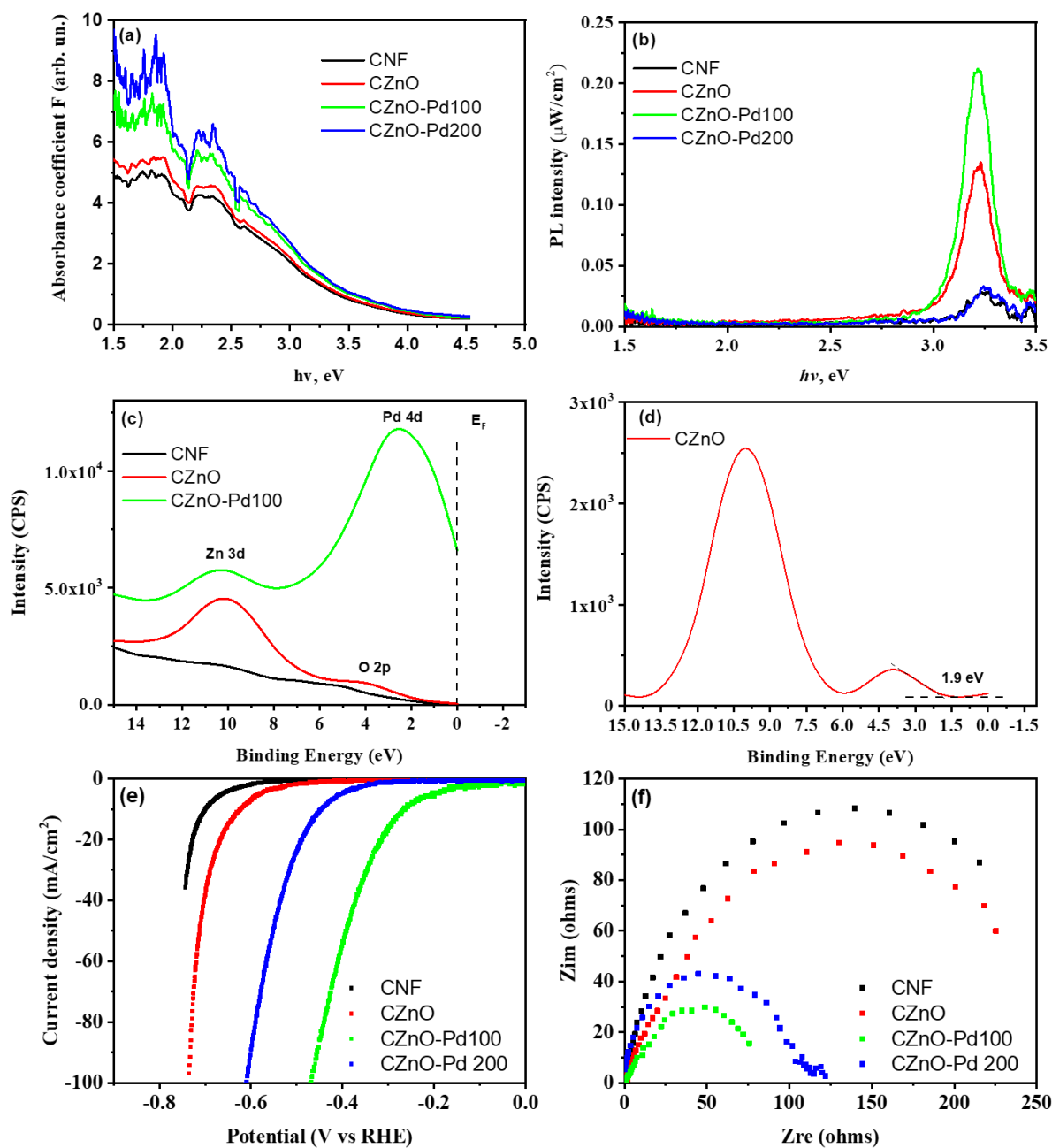
Figure 4: Absorbance spectra of CNF, CZnO, CZnO-Pd100 and CZnO-Pd200 nanofibers (a); PL
of CNF, CZnO, CZnO-Pd100 and CZnO-Pd200 nanofibers (b); VB-XPS of CNF, CZnO, CZnO-
Pd100 (c); Zooming of VB-XPS of CZnO (d); HER of CNF, CZnO, CZnO-Pd100 and CZnO-
Pd200 nanofibers (e); and EIS of CNF, CZnO, CZnO-Pd100 and CZnO-Pd200 nanofibers (f).

400

3.2 PEC degradation of paracetamol

The results for the PEC degradation of paracetamol using the prepared photoanode are presented

in Figures 5a-d. After 150 min, total removal (100%) of paracetamol was achieved using CZnO-

Pd100 anode (Fig 5a) with an applied current of 10 mA cm^{-2} (corresponding to 4.2 V). The

incorporation of Pd on the surface of ZnO/CNFs led to this impressive result because the CZnO

anode achieved just $56.40 \pm 2.10\%$ PEC removal of paracetamol after 150 min. This could be due

to the fact that transition metals improve the photocatalytic efficiencies of semiconductors by

increasing their light absorptivity and limiting spontaneous recombination. This is in line with

previous studies where doping ZnO with Pd has also been reported to increase the photocatalytic

efficiency of ZnO [92,93]. However, with CZnO-Pd200 photoanode, the percentage removal was

about $80.00 \pm 0.20\%$ after 150 min, and this revealed that the excessive amount of Pd in the

composite material could diminish its efficiency. The CZnO-Pd100 photoanode was subsequently

used to access the degradation of paracetamol through an electrochemical oxidation and

photocatalytic process in order to establish the superiority of PEC process. As shown in Figure 5b,

in the absence of light, the percentage removal of paracetamol decreased to about 82.20 ± 0.14 %

after 3 h, and this revealed that irradiation greatly enhanced the efficiency of the electrode. On the

other hand, when the degradation experiment was performed without applying an external current

(photocatalysis), the percentage removal reduced drastically to $14.30 \pm 0.12\%$. The lower

efficiency of the electrode in photocatalysis further showed that the applied current in the PEC

process remarkably improve the performance of the electrode by promoting efficient charge

separation since it provides a driving force for the photogenerated electron to move away from the

422   anode surface. Additionally, anodic oxidation of the paracetamol was also possible with the

423   application of external current.

424   In order to confirm the dependence of the PEC degradation process on the applied current, the

425   experiments were also performed with the application of 5 mA cm^{-2} (3.3 V) and compared with

426   the results obtained with 10 mA cm^{-2}. As presented in Figure 5c, at lower applied current (5 mA

427   cm^{-2}), the percentage of paracetamol degradation was reduced to $78.11 \pm 0.20\%$ after 150 min.

428   This clearly showed that the magnitude of applied current also has an effect on the separation of

429   photogenerated electron-hole pairs within ZnO. The space charge region and Helmholtz layer on

430   the surface of the photoanode largely determine the mobility of photogenerated charge carriers.

431   Applied current increases the width of the charge region, and when this happens, the spontaneous

432   recombination of photogenerated carriers is reduced [45]. An increase in the magnitude of applied

433   current could increase the width of the space charge region, and this evidently led to an increase

434   in percentage removal of paracetamol when the current was increased from 5 mA cm^{-2} to 10 mA

435   cm^{-2}. However, too high applied current promotes oxygen generation, which decreases PEC

436   degradation performance and could also affect the integrity of the electrode.

437   Kinetics study was also performed by fitting the experimental data into the pseudo second order

438   reaction kinetics model. The apparent rate constants were obtained from the slope of the plots of

439    $\ln C_o/C_t$ versus time (Figure 5d). In the PEC degradation processes using different photoanodes,

440   the apparent rate constants were 7.88×10^{-4} min^{-1}, 6.94×10^{-3} min^{-1} and 9.10×10^{-3} min^{-1} for CZnO,

441   CZnO-Pd200 and CZnO-Pd100 respectively. The highest rate constant obtained using CZnO-

442   Pd100 revealed that the PEC degradation is fastest using this electrode in addition to the highest

443   percentage removal obtained. Furthermore, the kinetics of photocatalytic, electrochemical (EC)

444   and PEC degradation were also studied using the CZnO-Pd100 electrode. It was found that the

445 order of increasing apparent rate constant was photocatalytic < electrochemical < PEC degradation

446 and this also showed that a combination of photocatalysis and electrochemical degradation in the

447 PEC process facilitated the fast rate at which paracetamol molecules were degraded. To further

448 justify the improved performance obtained through the incorporation of visible light irradiation

449 (photocatalysis) with applied external electric current, the degree of electrochemical enhancement

450 (E) and the degree of process synergy (S) were obtained using equations 3 and 4 respectively [94].

451 $$E = (K_{PEC} - K_{PC})/K_{PEC} \qquad\qquad\qquad (3)$$

452 $$S = (K_{PEC} - (K_{PC} + K_{EC}))/K_{PEC} \qquad\qquad (4)$$

453 Where K_{PC}, K_{EC}, and K_{PEC} are apparent rate constants for photocatalytic (7.883 x 10^{-4} min^{-1}),

454 electrochemical (5.37 x 10^{-3} min^{-1}) and PEC degradation (9.710 x 10^{-3} min^{-1}) of paracetamol,

455 respectively. The degree of electrochemical enhancement was calculated to be 0.91 (91%), which

456 established that the application of electric current has a tremendous impact on the PEC process,

457 and the percentage removal obtained with electrochemical degradation likewise justify this. In line

458 with this, the degree of process synergy calculated (0.323) was obviously greater than zero, which

459 confirmed that the improved performance obtained with PEC degradation is more than the

460 summation of the individual electrochemical and photocatalytic degradation process, revealing

461 that the introduction of applied electric current with photocatalysis result in a synergistic effect

462 and not cumulative/summation effect [94,95].

463 The catalytic performance of ZnO/Pd depends on ratio between Pd thickness and concentration of

464 active sites at ZnO/Pd interface [82]. It was shown that catalytic performance as a function of Pd

465 concentration had maximum between 0% Pd and 18% Pd loading. Higher concentration of Pd

466 restricts the role of metal oxide component in photocatalysis and therefore reduces total

467   photocatalytic effectiveness. This was in agreement with the results obtained from the PL spectra

468   discussed earlier where increase in Pd loading resulted in light scattering effect on the surface of

469   the catalyst, thereby diminishing its photocatalytic activity.

470   In the present work, ZnO-Pd100 samples showed higher performance compared to ZnO-Pd200

471   due to higher concentration of active sites. This was confirmed by optical characterizations

472   (photoluminescence) where, we can get highly efficiency at the certain amount of Pd active sites

473   (CZnO-Pd100).

474
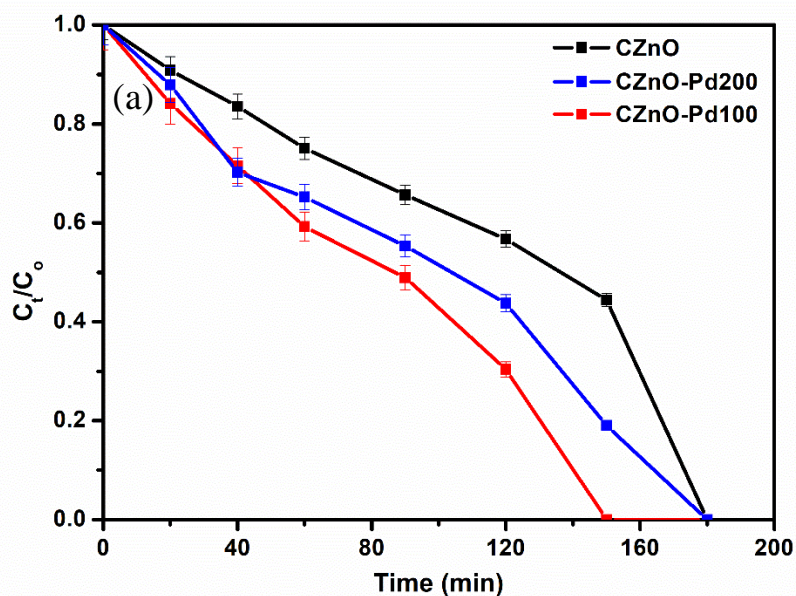
475

476

477

478

479

480
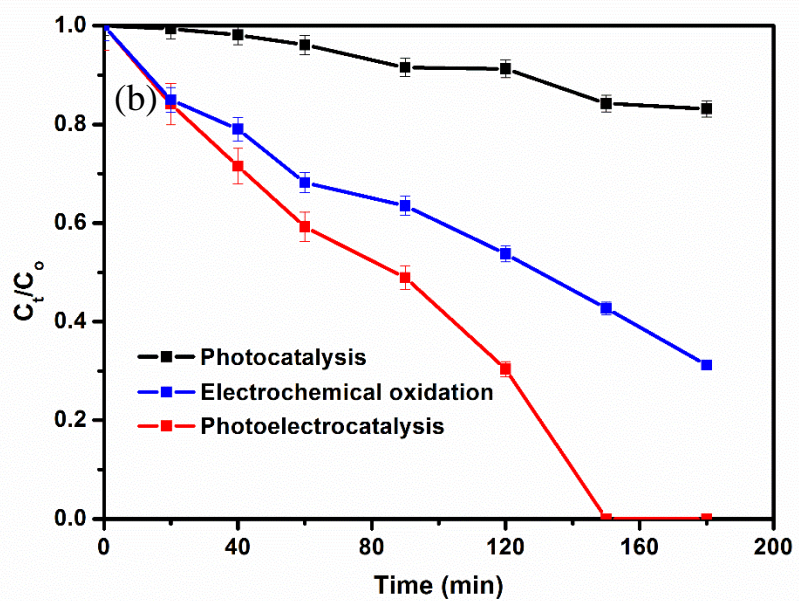
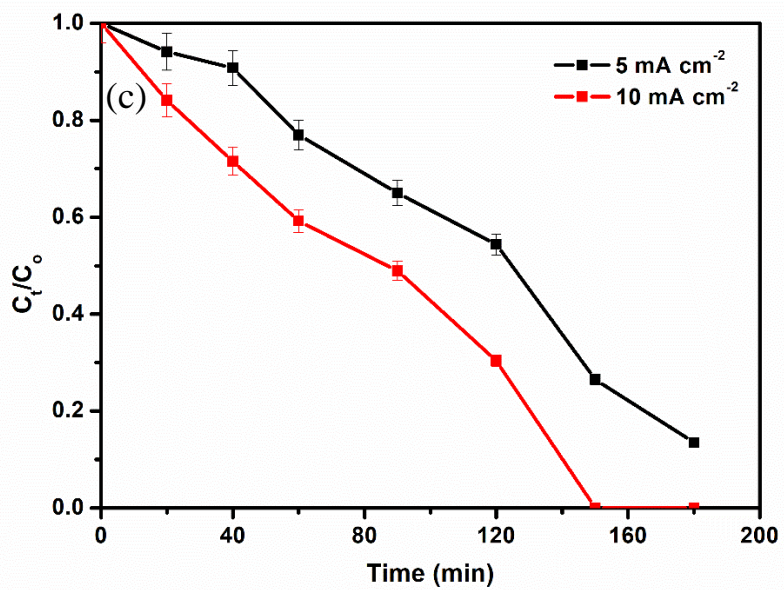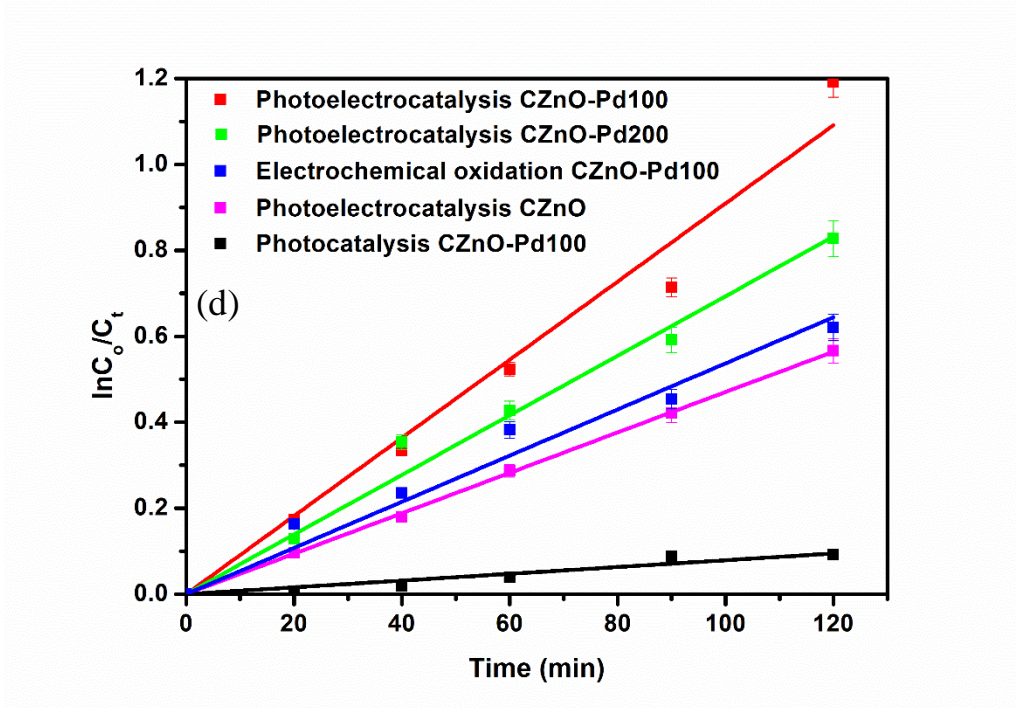**Figure 5**: Normalized concentration decay versus time plot for PEC degradation of paracetamol using (a) CZnO, CZnO-Pd100 and CZnO-Pd200; (b) Photocatalysis, electrochemical oxidation and photoelectrocatalysis using CZnO-Pd100; (c) Photoelectrocatalysis at different current densities using CZnO-Pd100; (d) Corresponding kinetics plot for the processes at 10 mAcm^{-2} (0.1 mM paracetamol; pH 7; 50 mM Na_2SO_4)

3.2.1 TOC removal and reusability of the electrode

In PEC degradation of organics, similar to other advanced oxidation processes, it is envisaged that the total mineralization of organics to water and carbon dioxide would occur after some period of reaction. In order to quantify the extent of mineralization of paracetamol using the composite electrode of CZnO-Pd100, the total organic carbon (TOC) content was measured as the PEC process progressed. As shown in Figure 6a, the percentage of TOC removal was approximately

493   71.20 ± 0.31% after 4 h. This clearly revealed that significant mineralization of paracetamol

494   molecules occurred in the PEC degradation. From the TOC results obtained, it became obvious

495   that the paracetamol was broken down totally to other smaller organics first, and this accounted

496   for the total removal of paracetamol achieved within 150 min. Since complete removal of TOC

497   was not recorded, smaller chain aliphatic organic acids such as fumaric, oxalic, acetic and maleic

498   acids, which are by products of paracetamol degradation, were still present in the solution [96,97].

499   Additionally, the corresponding calculated mineralization current efficiency (MCE%) was found

500   to decrease progressively with time from 15.10 ± 0.23% at 1 h to about 6.34 ± 0.03% after 4 h

501   (Figure 6b). This suggests a gradual reduction in the oxidation ability of the process, which could

502   be due to the generation of highly resistant short-chain hydrocarbon as by-products [98]. The

503   reduction in the organic content over a prolonged period could also limit the mass transport as well

504   as facilitating counterproductive reactions such as dimerization of hydroxyl radicals [99].

505   A desirable attribute of a potential photoanode for industrial water treatment applications is ease

506   of reusability. The reusability and stability of the CZnO-Pd100 anode were accessed by using the

507   electrode consecutively for eight times (8 runs or cycles) and recording the percentage removal

508   after 2 h (Figure 6c). After each run, the electrode was simply rinsed with deionized water and air-

509   dried overnight, unlike in some water treatment techniques where the recovery of the material is

510   often tedious and involves the use of strong chemicals [82,83]. After the eighth run, the difference

511   in the percentage removal was less than 4%, which confirmed the reusability of the anode. In

512   addition, we can note also that the crystallinity and the electronic state of CZnO-Pd100 nanofibers

513   (Figure S3) did not change after photoelectrocatalytic reaction as confirmed by XRD and XPS.

514

515

516

517

518

519
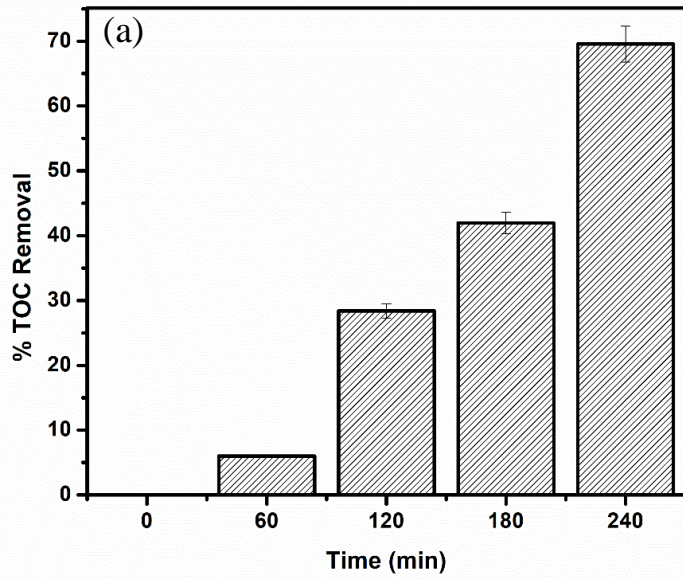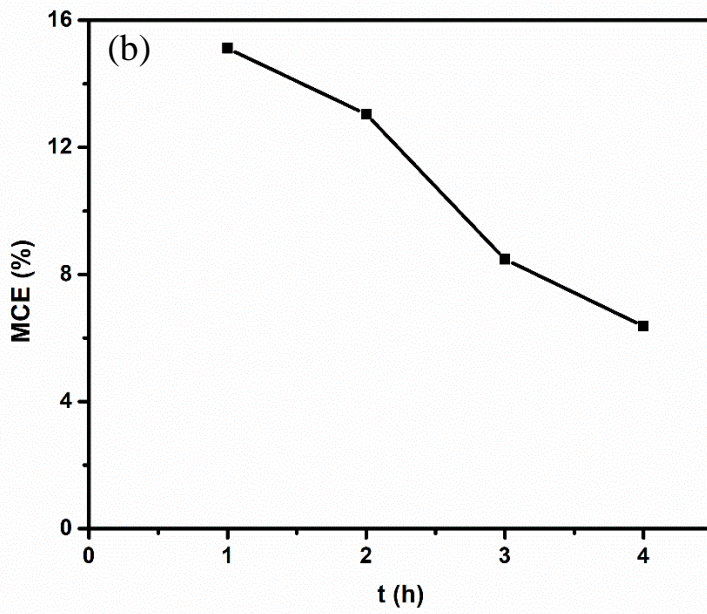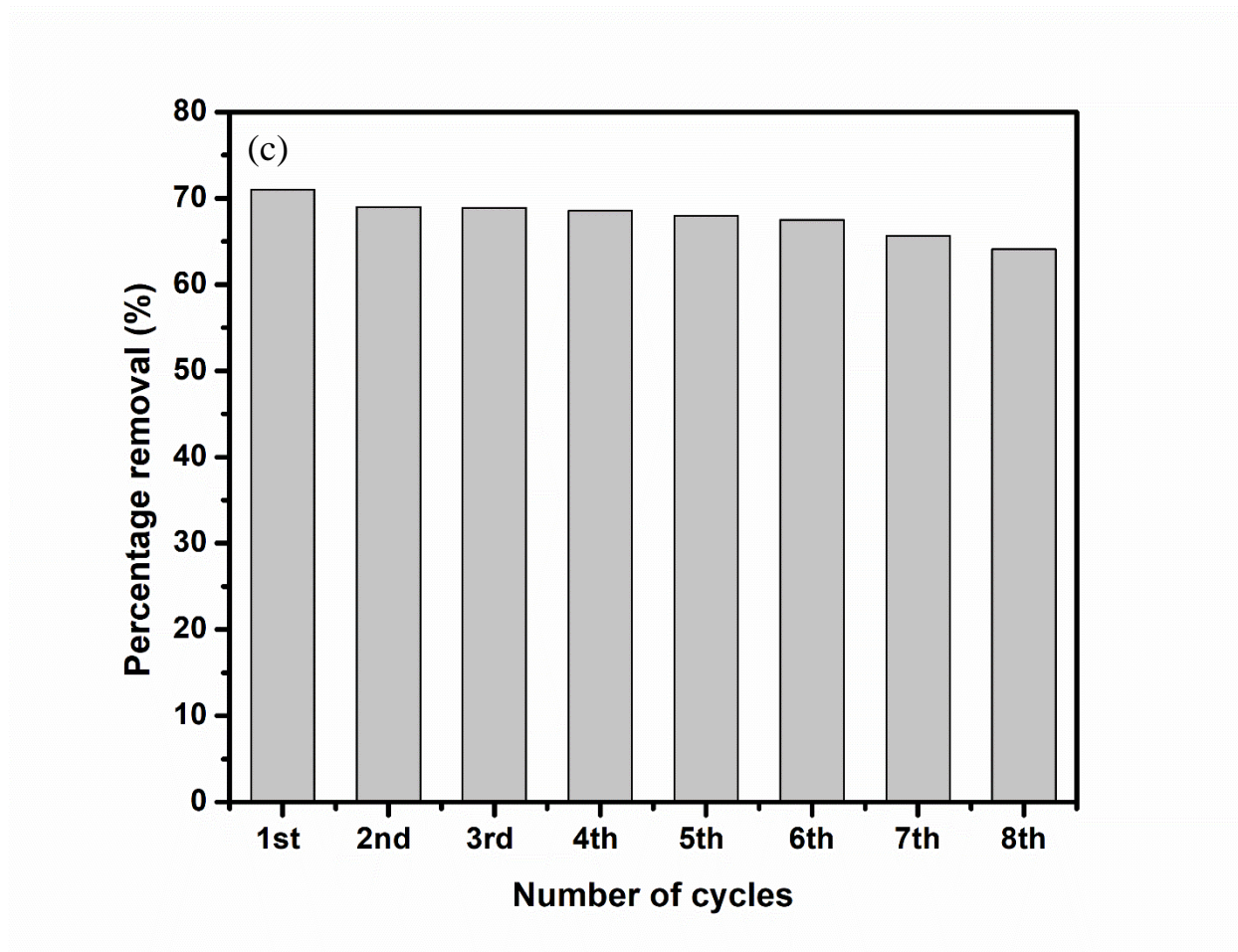
Figure 6: (a) Percentage total organic carbon removal in the PEC degradation of paracetamol; (b) Corresponding percentage mineralization current efficiency with time; (c) Reusability tests (0.1 mM paracetamol; pH 7; CZnO-Pd100; 10 mA cm^{-2})

3.2.2 Scavenger studies and proposed degradation mechanism

In a typical PEC degradation process, in addition to hydroxyl radicals, other reactive species such as photogenerated holes and superoxide radicals also contribute at different degrees to the

527 mineralization of organic molecules [98]. The stepwise formations of these reactive species and

528 their reaction with paracetamol molecules are presented in equations 5 – 10:

529 $$hv + CZnO/Pd \rightarrow CZnO/Pd\ (h^+ + e^-) \qquad (5)$$

530 $$e^- + O_2 \rightarrow {}^\bullet O_2^- \qquad (6)$$

531 $$h^+ + H_2O \rightarrow {}^\bullet OH + H^+ \qquad (7)$$

532 $${}^\bullet OH + paracetamol \rightarrow CO_2 + H_2O + intermediate\ products \qquad (8)$$

533 $${}^\bullet O_2^- + paracetamol \rightarrow CO_2 + H_2O + intermediate\ products \qquad (9)$$

534 $$h^+ + paracetamol \rightarrow CO_2 + H_2O + intermediate\ products \qquad (10)$$
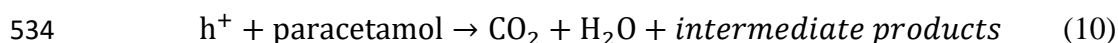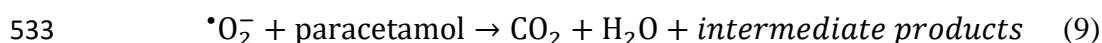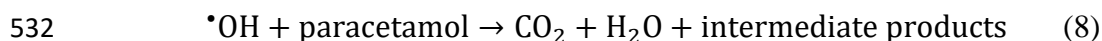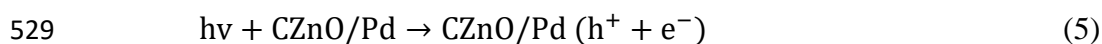
535

536 Trapping experiments were therefore conducted to understand the specific roles of hydroxyl

537 radicals, photogenerated holes and superoxide radicals in the PEC degradation of paracetamol by

538 the addition of 0.001 M Isopropanol (IPA), 0.02 M p-benzoquinone (p-BQ) and 0.01 M

539 ethylenediaminetetraacetate (EDTA) to the electrolytic solution to suppress the effect of hydroxyl

540 radicals, superoxide radicals and holes respectively [98,99]. As presented in Figure 7, upon the

541 addition of EDTA, the percentage removal of paracetamol dropped significantly to $18.70 \pm 0.20\%$

542 after 2 h. This revealed that separated photogenerated holes played a major role in the

543 mineralization of paracetamol. This is in agreement with literatures that photogenerated holes can

544 directly oxidize organics in solution rather than generating hydroxyl radicals first in PEC systems

545 [23]. Additionally, hydroxyl radicals also contributed to the total percentage removal obtained

546 because when the reaction was done in the presence of isopropanol, the percentage removal was

547 $35.10 \pm 1.40\%$. On the other hand, in the presence of p-BQ, substantial degradation percentage

548 was still recorded which clearly revealed that superoxide radicals played a far less role in the

549 degradation process. With these findings, it can be established that the degradation of paracetamol

550   molecules using the CZnO-Pd photoanode depends largely on the photogenerated holes.

551   Generally, when a semiconductor is irradiated with light of appropriate energy, the photo excited

552   electrons transfer from the valence band to the conduction band while holes occupy the valence

553   band. However, the photogenerated electrons fall back within a short time to recombine with the

554   photogenerated holes and this prevents the photogenerated holes from reacting with water

555   molecules to produce hydroxyl radicals or directly oxidizing organic molecules present in the

556   solution. In the case of CZnO-Pd photoanode, the efficiency of ZnO is greatly enhanced through

557   improve charge carrier separation due to the presence of Pd. This is because when Pd is in contact

558   with ZnO, a Schottky barrier is created which facilitated the migration of photogenerated holes

559   from the conduction band of ZnO to Pd metal. Consequently, more photogenerated holes are

560   readily available in the valence band of ZnO which either react directly with the paracetamol

561   molecules or with water molecules to produce hydroxyl radicals which then oxidize the

562   paracetamol to water and carbon dioxide. It is also important to note that electrons migrate from

563   the photoanode to the cathode. These electrons could also produce superoxide radicals which can

564   contribute to the degradation of the paracetamol molecules, however, the trapping experiments

565   revealed that the contribution of superoxide radicals is negligible. There is also a possibility of the

566   generation of hydrogen molecules on the cathode by the reactions of electrons with water

567   molecules [100]. The proposed mechanism for the production of oxidants and degradation of

568   paracetamol molecules is illustrated in the schematic diagram presented in Figure 7b (Mechanism

569   PEC degradation process using CZnO-Pd100 photoanode).

570   .
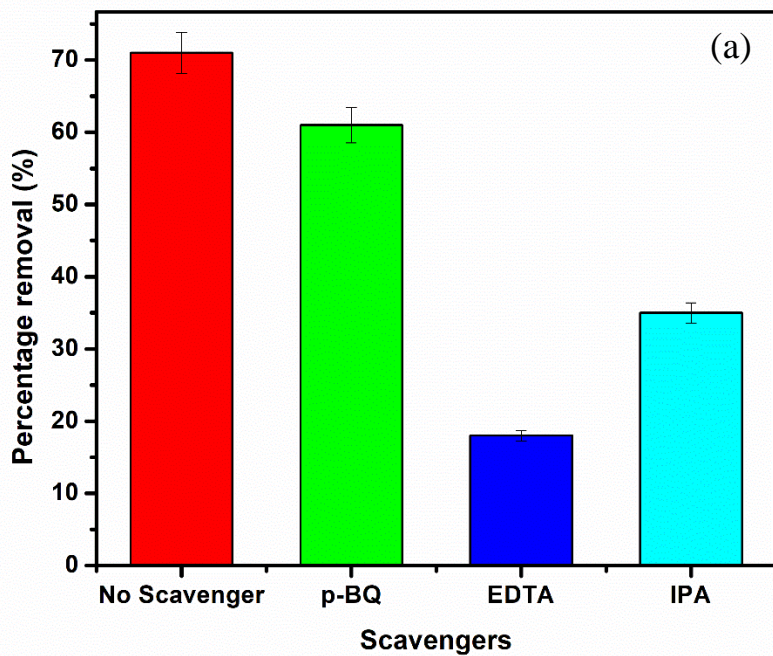
571

572
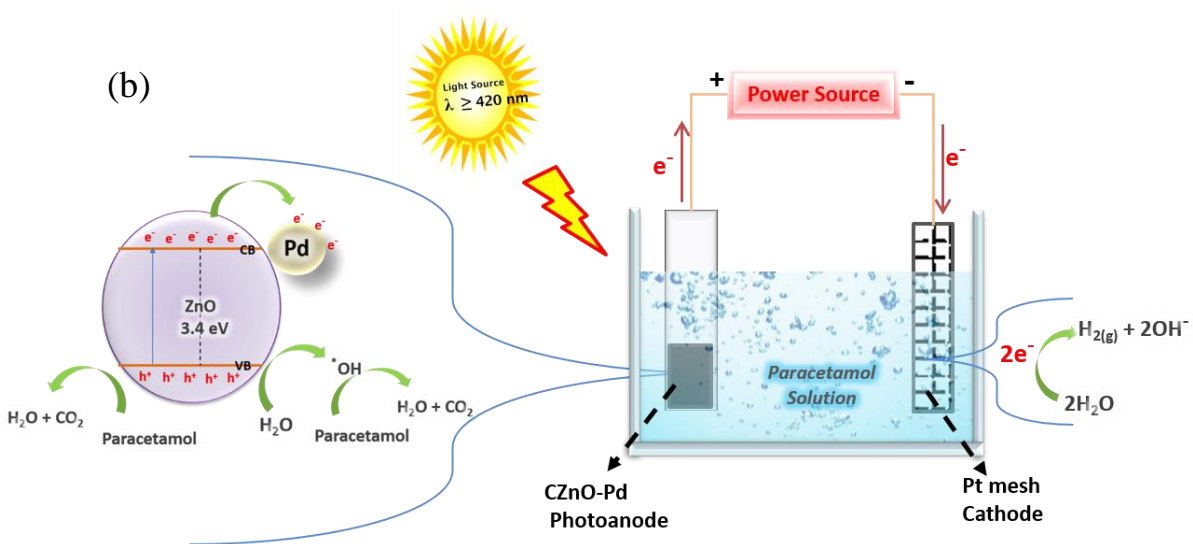
573

574 **Figure 7**: (a) PEC degradation of paracetamol in the presence on scavengers; (b) Mechanism PEC

575 degradation process using CZnO-Pd100 photoanode (2 h; 0.1 mM paracetamol; 10 mA cm^{-2};

576 CZnO-Pd100)

577   **3.2.3 Comparison with previous studies**

578   Several kinds of semiconductor photoanodes have been explored for the PEC degradation of

579   pharmaceuticals. To clearly justify the performance of the CZnO-Pd photoanode, the results

580   obtained were compared with earlier literatures on PEC degradation of paracetamol. As presented

581   in Table 1, the percentage removal as well as TOC removal obtained with the present electrode

582   compares well with the previous studies and in fact, in some cases the electrode performed better

583   than other earlier reported electrodes. Therefore, CZnO-Pd can be a suitable photoanode for the

584   PEC removal of paracetamol molecules in wastewater.

585   **Table 1:** Comparison of electrode performance with previous studies

Photoanode	Paracetamol concentration (mgL^{-1})	Percentage Removal	%TOC removal	References
Au-TiO$_2$	78.5	66% after 3 h	20% after 3 h	[101]
TiO$_2$	60	100% after 70 min	-	[102]
BiVO$_4$/BiOI	10	68% after 2 h	59% after 2 h	[103]
TiO$_2$	40	45% after 4 h	21% after 4 h	[104]
CZnO-Pd	151	100% after 150 min	71% after 4 h	Present study

586

587   **Conclusion**

588   In this work, successful preparation of Pd loaded zinc oxide carbon nanofibers (CZnO-Pd) was

589   achieved through electrospinning and atomic layer deposition. Results from the structural and

590   morphological characterization revealed that amorphous ZnO nanoparticles were homogenously

591   deposited on the surface of the carbon nanofibers while spherical metallic Pd nanoparticles were

592 deposited on the edge/shell of the nanofibers to form a coaxial or core/shell structure. The prepared

593 material (CZnO-Pd100) displayed good absorbance of photons in the visible light region due to

594 the presence of metallic Pd. However, the visible light absorption of the material decreased with

595 high content of Pd nanoparticles (ZCnO-Pd200). Similar trend was observed when the prepared

596 materials were applied for the photoelectrocatalytic removal of paracetamol. Total removal was

597 achieved in less than 3 h with $71.20 \pm 0.31\%$ TOC removal after 4 h with the use of CZnO-Pd100

598 while the percentage removal obtained with CZnO-Pd200 was lower due higher content of Pd

599 particles which decreased the photocatalytic active of the semiconductor. Additionally, the rate of

600 the PEC degradation process of paracetamol using the CZnO-Pd100 photoanode was fast and the

601 mechanism of the reaction suggests that both photogenerated holes and hydroxyl radicals played

602 substantial role in the degradation of the paracetamol molecules. Overall, the CZnO-Pd material

603 has a great potential as photoanode for the mineralization of organic pollutants in wastewater.

604

613

References

[1]   C. Wu, C. Maurer, Y. Wang, S. Xue, D.L. Davis, Water pollution and human health in
      China, Environ. Health Perspect. 107 (1999) 251–256. doi:10.1289/ehp.99107251.

[2]   A.S. Morshedy, H.R. Ali, A.A. Nada, A.M. Rabie, H.H. El-Maghrabi, Highly efficient
      Imprinted Polymer Nanocomposites for photocatalytic desulfurization of real diesel fuel,
      Environ. Technol. Innov. (2020). doi:10.1016/j.eti.2020.101206.

[3]   A.A. Nada, H.R. Tantawy, M.A. Elsayed, M. Bechelany, M.E. Elmowafy, Elaboration of
      nano titania-magnetic reduced graphene oxide for degradation of tartrazine dye in aqueous
      solution, Solid State Sci. 78 (2018). doi:10.1016/j.solidstatesciences.2018.02.014.

[4]   R. Elshypany, H. Selim, K. Zakaria, A.H. Moustafa, S.A. Sadeek, S.I. Sharaa, P. Raynaud,
      A.A. Nada, Magnetic ZnO Crystal Nanoparticle Growth on Reduced Graphene Oxide for
      Enhanced Photocatalytic Performance under Visible Light Irradiation, (2021).

[5]   H.H. El-Maghrabi, A.A. Al-Kahlawy, A.A. Nada, T. Zaki, Photocorrosion resistant
      Ag2CO3@Fe2O3/TiO2-NT nanocomposite for efficient visible light photocatalytic
      degradation activities, J. Hazard. Mater. (2018). doi:10.1016/j.jhazmat.2018.08.002.

[6]   A.A. Nada, M.F. Bekheet, S. Roualdes, A. Gurlo, A. Ayral, Functionalization of MCM-41
      with titanium oxynitride deposited via PECVD for enhanced removal of methylene blue,
      J. Mol. Liq. (2019). doi:10.1016/j.molliq.2018.10.154.

[7]   A.L. Spongberg, J.D. Witter, Pharmaceutical compounds in the wastewater process stream
      in Northwest Ohio, Sci. Total Environ. 397 (2008) 148–157.
      doi:10.1016/j.scitotenv.2008.02.042.

36

635   [8]   D.G.J. Larsson, C. De Pedro, N. Paxeus, Effluent from drug manufactures contains

636   extremely high levels of pharmaceuticals, 148 (2007) 751–755.

637   doi:10.1016/j.jhazmat.2007.07.008.

638   [9]   H.H. El-Maghrabi, E.A. Nada, F.S. Soliman, Y.M. Moustafa, A.E.-S. Amin, One pot

639   environmental friendly nanocomposite synthesis of novel TiO2-nanotubes on graphene

640   sheets as effective photocatalyst, Egypt. J. Pet. 25 (2016) 575–584.

641   [10]   J. Wilkinson, P.S. Hooda, J. Barker, S. Barton, J. Swinden, Occurrence, fate and

642   transformation of emerging contaminants in water: An overarching review of the field,

643   Environ. Pollut. 231 (2017) 954–970. doi:10.1016/j.envpol.2017.08.032.

644   [11]   J. Fick, H. Söderström, R.H. Lindberg, C. Phan, M. Tysklind, D.G.J. Larsson,

645   Contamination of Surface, Ground, and Drinking Water From Pharmaceutical Production,

646   Environ. Toxicol. Chem. 28 (2009) 2522. doi:10.1897/09-073.1.

647   [12]   S. Mompelat, B. Le Bot, O. Thomas, Occurrence and fate of pharmaceutical products and

648   by-products, from resource to drinking water, Environ. Int. 35 (2009) 803–814.

649   doi:10.1016/j.envint.2008.10.008.

650   [13]   N. Serpone, Y.M. Artemev, V.K. Ryabchuk, A. V. Emeline, S. Horikoshi, Light-driven

651   advanced oxidation processes in the disposal of emerging pharmaceutical contaminants in

652   aqueous media: A brief review, Curr. Opin. Green Sustain. Chem. 6 (2017) 18–33.

653   doi:10.1016/j.cogsc.2017.05.003.

654   [14]   T.B. Devi, M. Ahmaruzzaman, Bio-inspired facile and green fabrication of

655   Au@Ag@AgCl core–double shells nanoparticles and their potential applications for

656   elimination of toxic emerging pollutants: A green and efficient approach for wastewater

657   treatment, Chem. Eng. J. 317 (2017) 726–741. doi:10.1016/j.cej.2017.02.082.

658   [15]   N. Kemper, Veterinary antibiotics in the aquatic and terrestrial environment, Ecol. Indic. 8

659   (2008) 1–13. doi:10.1016/j.ecolind.2007.06.002.

660   [16]   P. Välitalo, A. Kruglova, A. Mikola, R. Vahala, Toxicological impacts of antibiotics on

661   aquatic micro-organisms: A mini-review, Int. J. Hyg. Environ. Health. 220 (2017) 558–

662   569. doi:10.1016/j.ijheh.2017.02.003.

663   [17]   A.M. Deegan, B. Shaik, K. Nolan, K. Urell, M. Oelgemöller, J. Tobin, A. Morrissey,

664   Treatment options for wastewater effluents from pharmaceutical companies, Int. J.

665   Environ. Sci. Technol. 8 (2011) 649–666. doi:10.1007/BF03326250.

666   [18]   C. Trellu, B.P. Chaplin, C. Coetsier, R. Esmilaire, S. Cerneaux, C. Causserand, M. Cretin,

667   Electro-oxidation of organic pollutants by reactive electrochemical membranes,

668   Chemosphere. 208 (2018) 159–175. doi:10.1016/j.chemosphere.2018.05.026.

669   [19]   M.A. Oturan, J.J. Aaron, Advanced oxidation processes in water/wastewater treatment:

670   Principles and applications. A review, Crit. Rev. Environ. Sci. Technol. 44 (2014) 2577–

671   2641. doi:10.1080/10643389.2013.829765.

672   [20]   E. Brillas, I. Sirés, M.A. Oturan, Electro-fenton process and related electrochemical

673   technologies based on fenton's reaction chemistry, Chem. Rev. 109 (2009) 6570–6631.

674   doi:10.1021/cr900136g.

675   [21]   O. Monfort, G. Plesch, Bismuth vanadate-based semiconductor photocatalysts: a short

676   critical review on the efficiency and the mechanism of photodegradation of organic

677   pollutants, Environ. Sci. Pollut. Res. 25 (2018) 19362–19379. doi:10.1007/s11356-018-

678   2437-9.

679   [22] M. El Kateb, C. Trellu, A. Darwich, M. Rivallin, M. Bechelany, S. Nagarajan, S. Lacour,

680   N. Bellakhal, G. Lesage, M. Héran, M. Cretin, Electrochemical advanced oxidation

681   processes using novel electrode materials for mineralization and biodegradability

682   enhancement of nanofiltration concentrate of landfill leachates, Water Res. 162 (2019)

683   446–455. doi:10.1016/j.watres.2019.07.005.

684   [23] S. Garcia-Segura, E. Brillas, Applied photoelectrocatalysis on the degradation of organic

685   pollutants in wastewaters, J. Photochem. Photobiol. C Photochem. Rev. 31 (2017) 1–35.

686   doi:10.1016/j.jphotochemrev.2017.01.005.

687   [24] A.A. Nada, M. Nasr, R. Viter, P. Miele, S. Roualdes, M. Bechelany, Mesoporous

688   ZnFe2O4@TiO2 nanofibers prepared by electrospinning coupled to PECVD as highly

689   performing photocatalytic materials, J. Phys. Chem. C. (2017).

690   doi:10.1021/acs.jpcc.7b08567.

691   [25] M.G. Peleyeju, O.A. Arotiba, Recent trend in visible-light photoelectrocatalytic systems

692   for degradation of organic contaminants in water/wastewater, Environ. Sci. Water Res.

693   Technol. 4 (2018) 1389–1411. doi:10.1039/c8ew00276b.

694   [26] S. Kawrani, M. Boulos, M.F. Bekheet, R. Viter, A.A. Nada, W. Riedel, S. Roualdes, D.

695   Cornu, M. Bechelany, Segregation of copper oxide on calcium copper titanate surface

696   induced by Graphene Oxide for Water splitting applications, Appl. Surf. Sci. 516 (2020)

697   146051.

698   [27] S. Kawrani, A.A. Nada, M.F. Bekheet, M. Boulos, R. Viter, S. Roualdes, P. Miele, D.

699   Cornu, M. Bechelany, Enhancement of calcium copper titanium oxide

700   photoelectrochemical performance using boron nitride nanosheets, Chem. Eng. J. 389

701   (2020). doi:10.1016/j.cej.2020.124326.

702   [28]   O.A. Arotiba, B.O. Orimolade, B.A. Koiki, Visible Light Driven Photoelectrocatalytic

703   Semiconductor Heterojunction Anodes for Water Treatment Applications, Curr. Opin.

704   Electrochem. (2020) 1–10. doi:10.1016/j.coelec.2020.03.018.

705   [29]   R. Daghrir, P. Drogui, D. Robert, Photoelectrocatalytic technologies for environmental

706   applications, J. Photochem. Photobiol. A Chem. 238 (2012) 41–52.

707   doi:10.1016/j.jphotochem.2012.04.009.

708   [30]   A. Miquelot, L. Youssef, C. Villeneuve-Faure, N. Prud'Homme, N. Dragoe, A. Nada, V.

709   Rouessac, S. Roualdes, J. Bassil, M. Zakhour, In-and out-plane transport properties of

710   chemical vapor deposited TiO 2 anatase films, J. Mater. Sci. 56 (2021) 10458–10476.

711   [31]   B.O. Orimolade, O.A. Arotiba, An Exfoliated Graphite-Bismuth Vanadate Composite

712   Photoanode for the Photoelectrochemical Degradation of Acid Orange 7 Dye,

713   Electrocatalysis. 10 (2019) 429–435. doi:10.1007/s12678-019-00534-5.

714   [32]   Y. Zhou, X. Fan, G. Zhang, W. Dong, Fabricating MoS 2 nanoflakes photoanode with

715   unprecedented high photoelectrochemical performance and multi-pollutants degradation

716   test for water treatment, Chem. Eng. J. 356 (2019) 1003–1013.

717   doi:10.1016/j.cej.2018.09.097.

718   [33]   B.A. Koiki, B.O. Orimolade, B.N. Zwane, D. Nkosi, N. Mabuba, O.A. Arotiba, Cu2O on

719   anodised TiO2 nanotube arrays: A heterojunction photoanode for visible light assisted

720   electrochemical degradation of pharmaceuticals in water, Electrochim. Acta. 340 (2020)

721   135944. doi:10.1016/j.electacta.2020.135944.

40

722   [34]   M. Zhang, W. Pu, S. Pan, O.K. Okoth, C. Yang, J. Zhang, Photoelectrocatalytic activity of

723   liquid phase deposited α-Fe2O3 films under visible light illumination, J. Alloys Compd.

724   648 (2015) 719–725. doi:10.1016/j.jallcom.2015.07.026.

725   [35]   E.H. Umukoro, M.G. Peleyeju, J.C. Ngila, O.A. Arotiba, Towards wastewater treatment:

726   Photo-assisted electrochemical degradation of 2-nitrophenol and orange II dye at a

727   tungsten trioxide-exfoliated graphite composite electrode, Chem. Eng. J. 317 (2017) 290–

728   301. doi:10.1016/j.cej.2017.02.084.

729   [36]   M. Pirhashemi, A. Habibi-Yangjeh, S. Rahim Pouran, Review on the criteria anticipated

730   for the fabrication of highly efficient ZnO-based visible-light-driven photocatalysts, J. Ind.

731   Eng. Chem. 62 (2018) 1–25. doi:10.1016/j.jiec.2018.01.012.

732   [37]   A.J. de Walle, C.G. Van, Fundamentals of zinc oxide as a semiconductor, Reports Prog.

733   Phys. 72 (2009) 126501.

734   [38]   A.B. Djurišić, X. Chen, Y.H. Leung, A. Man Ching Ng, ZnO nanostructures: Growth,

735   properties and applications, J. Mater. Chem. 22 (2012) 6526–6535.

736   doi:10.1039/c2jm15548f.

737   [39]   H. Wang, S. Cao, B. Yang, H. Li, M. Wang, X. Hu, K. Sun, Z. Zang, NH 4 Cl-Modified

738   ZnO for High-Performance CsPbIBr 2 Perovskite Solar Cells via Low-Temperature

739   Process, Sol. RRL. 4 (2020) 1900363. doi:10.1002/solr.201900363.

740   [40]   H. Wang, P. Zhang, Z. Zang, High performance CsPbBr3 quantum dots photodetectors by

741   using zinc oxide nanorods arrays as an electron-transport layer, Appl. Phys. Lett. 116

742   (2020) 162103. doi:10.1063/5.0005464.

743   [41]   J.S. Yang, J.J. Wu, Low-potential driven fully-depleted BiVO4/ZnO heterojunction

744   nanodendrite array photoanodes for photoelectrochemical water splitting, Nano Energy.

745   32 (2017) 232–240. doi:10.1016/j.nanoen.2016.12.039.

746   [42]   W. Chen, W. Wu, W. Yang, J. Zhao, M. Xiao, W. Kong, CdCl2-assisting heat-treatment:

747   Enhanced photoelectrocatalytic hydrogen generation and stability of CdS/ZnO

748   nanoheterojunction arrays, Int. J. Hydrogen Energy. 43 (2018) 9969–9977.

749   doi:10.1016/j.ijhydene.2018.04.045.

750   [43]   T.N. Trung, D.B. Seo, N.D. Quang, D. Kim, E.T. Kim, Enhanced photoelectrochemical

751   activity in the heterostructure of vertically aligned few-layer MoS2 flakes on ZnO,

752   Electrochim. Acta. 260 (2018) 150–156. doi:10.1016/j.electacta.2017.11.089.

753   [44]   A.P.P. da Rosa, R.P. Cavalcante, T.F. da Silva, F. Gozzi, C. Byrne, E. McGlynn, G.A.

754   Casagrande, S.C. de Oliveira, A.M. Junior, Photoelectrocatalytic Degradation of

755   Methylene Blue Using ZnO Nanorods Fabricated on Silicon Substrates, J. Nanosci.

756   Nanotechnol. 20 (2019) 1177–1188. doi:10.1166/jnn.2020.16961.

757   [45]   M. Hosseini, A. Esrafili, M. Farzadkia, M. Kermani, M. Gholami, Degradation of

758   ciprofloxacin antibiotic using photo-electrocatalyst process of Ni-doped ZnO deposited by

759   RF sputtering on FTO as an anode electrode from aquatic environments: Synthesis,

760   kinetics, and ecotoxicity study, Microchem. J. 154 (2020) 104663.

761   doi:10.1016/j.microc.2020.104663.

762   [46]   J. Feng, Y. Tian, O.K. Okoth, L. Cheng, J. Zhang, Liquid Phase Deposition of Nickel-

763   Doped ZnO Film with Enhanced Visible Light Photoelectrocatalytic Activity, J.

764   Electrochem. Soc. 166 (2019) H685–H690. doi:10.1149/2.0361914jes.

765   [47]   W. Fei, H. Li, N. Li, D. Chen, Q. Xu, H. Li, J. He, J. Lu, Facile fabrication of ZnO/MoS2

766   p-n junctions on Ni foam for efficient degradation of organic pollutants through

767   photoelectrocatalytic process, Sol. Energy. 199 (2020) 164–172.

768   doi:10.1016/j.solener.2020.02.037.

769   [48]   J. Feng, L. Cheng, J. Zhang, O.K. Okoth, F. Chen, Preparation of BiVO4/ZnO composite

770   film with enhanced visible-light photoelectrocatalytic activity, Ceram. Int. 44 (2018)

771   3672–3677. doi:10.1016/j.ceramint.2017.11.124.

772   [49]   B.O. Orimolade, B.A. Koiki, B.N. Zwane, G.M. Peleyeju, N. Mabuba, O.A. Arotiba,

773   Interrogating solar photoelectrocatalysis on an exfoliated graphite–BiVO $_4$ /ZnO

774   composite electrode towards water treatment, RSC Adv. 9 (2019) 16586–16595.

775   doi:10.1039/C9RA02366F.

776   [50]   J. Wang, H. Zhu, J.D. Chen, B. Zhang, M. Zhang, L.N. Wang, M.L. Du, Small and well-

777   dispersed Cu nanoparticles on carbon nanofibers: Self-supported electrode materials for

778   efficient hydrogen evolution reaction, Int. J. Hydrogen Energy. 41 (2016) 18044–18049.

779   doi:10.1016/j.ijhydene.2016.08.058.

780   [51]   J. Wang, H. Zhu, D. Yu, J.W. Chen, J.D. Chen, M. Zhang, L.N. Wang, M.L. Du,

781   Engineering the Composition and Structure of Bimetallic Au-Cu Alloy Nanoparticles in

782   Carbon Nanofibers: Self-Supported Electrode Materials for Electrocatalytic Water

783   Splitting, ACS Appl. Mater. Interfaces. 9 (2017) 19756–19765.

784   doi:10.1021/acsami.7b01418.

785   [52]   M. Najem, A.A. Nada, M. Weber, S. Sayegh, A. Razzouk, C. Salameh, C. Eid, M.

786   Bechelany, Palladium/Carbon Nanofibers by Combining Atomic Layer Deposition and

43

787   Electrospinning for Organic Pollutant Degradation, Materials (Basel). 13 (2020) 1947.

788   [53]   C. Zhou, C. Lai, D. Huang, G. Zeng, C. Zhang, Highly porous carbon nitride by

789   supramolecular preassembly of monomers for photocatalytic removal of sulfamethazine

790   under visible light driven, Appl. Catal. B Environ. 220 (2018) 202–210.

791   doi:10.1016/j.apcatb.2017.08.055.

792   [54]   A. Barhoum, H.H. El-Maghrabi, I. Iatsunskyi, E. Coy, A. Renard, C. Salameh, M. Weber,

793   S. Sayegh, A.A. Nada, S. Roualdes, M. Bechelany, Atomic layer deposition of Pd

794   nanoparticles on self-supported carbon-Ni/NiO-Pd nanofiber electrodes for

795   electrochemical hydrogen and oxygen evolution reactions, J. Colloid Interface Sci. 569

796   (2020) 286–297. doi:10.1016/j.jcis.2020.02.063.

797   [55]   H.H. El-Maghrabi, A.A. Nada, S. Roualdes, M.F. Bekheet, Design of Ni/NiO–TiO2/rGO

798   nanocomposites on carbon cloth conductors via PECVD for electrocatalytic water

799   splitting, Int. J. Hydrogen Energy. 45 (2020) 32000–32011.

800   [56]   T. Cai, Y. Huang, M. Huang, Y. Xi, D. Pang, W. Zhang, Enhancing oxygen reduction

801   reaction of supercapacitor microbial fuel cells with electrospun carbon nanofibers

802   composite cathode, Chem. Eng. J. 371 (2019) 544–553. doi:10.1016/j.cej.2019.04.025.

803   [57]   Q. Ding, M. Liu, Y.-E. Miao, Y. Huang, T. Liu, Electrospun nickel-decorated carbon

804   nanofiber membranes as efficient electrocatalysts for hydrogen evolution reaction,

805   Electrochim. Acta. 159 (2015) 1–7. doi:10.1016/J.ELECTACTA.2015.01.197.

806   [58]   M. El-Sayed, A.A. Nada, Polyethylenimine −functionalized amorphous carbon fabricated

807   from oil palm leaves as a novel adsorbent for Cr(VI) and Pb(II) from aqueous solution, J.

808   Water Process Eng. (2017). doi:10.1016/j.jwpe.2017.02.012.

809 [59] A.A. Nada, M.F. Bekheet, R. Viter, P. Miele, S. Roualdes, M. Bechelany, BN/GdxTi (1-x)

810 O (4-x)/2 nanofibers for enhanced photocatalytic hydrogen production under visible light,

811 Appl. Catal. B Environ. 251 (2019) 76–86. doi:10.1016/j.apcatb.2019.03.043.

812 [60] H.H. El-Maghrabi, A.A. Nada, M.F. Bekheet, S. Roualdes, W. Riedel, I. Iatsunskyi, E.

813 Coy, A. Gurlo, M. Bechelany, Coaxial nanofibers of nickel/gadolinium oxide/nickel oxide

814 as highly effective electrocatalysts for hydrogen evolution reaction, J. Colloid Interface

815 Sci. (2020). doi:https://doi.org/10.1016/j.jcis.2020.11.103.

816 [61] M. Weber, A. Julbe, A. Ayral, P. Miele, M. Bechelany, Atomic Layer Deposition for

817 Membranes: Basics, Challenges, and Opportunities, Chem. Mater. 30 (2018) 7368–7390.

818 doi:10.1021/acs.chemmater.8b02687.

819 [62] O. Graniel, M. Weber, S. Balme, P. Miele, M. Bechelany, Atomic layer deposition for

820 biosensing applications, Biosens. Bioelectron. 122 (2018) 147–159.

821 doi:10.1016/j.bios.2018.09.038.

822 [63] M. Weber, N. Tuleushova, J. Zgheib, C. Lamboux, I. Iatsunskyi, E. Coy, V. Flaud, S.

823 Tingry, D. Cornu, P. Miele, Enhanced electrocatalytic performance triggered by

824 atomically bridged boron nitride between palladium nanoparticles and carbon fibers in

825 gas-diffusion electrodes, Appl. Catal. B Environ. 257 (2019) 117917.

826 [64] E.J. Ruiz, A. Hernández-Ramírez, J.M. Peralta-Hernández, C. Arias, E. Brillas,

827 Application of solar photoelectro-Fenton technology to azo dyes mineralization: Effect of

828 current density, Fe2+ and dye concentrations, Chem. Eng. J. 171 (2011) 385–392.

829 doi:10.1016/j.cej.2011.03.004.

830 [65] T.X. Huong Le, L.F. Dumée, S. Lacour, M. Rivallin, Z. Yi, L. Kong, M. Bechelany, M.

831 Cretin, Hybrid graphene-decorated metal hollow fibre membrane reactors for efficient

832 electro-Fenton - Filtration co-processes, J. Memb. Sci. 587 (2019) 117182.

833 doi:10.1016/j.memsci.2019.117182.

834 [66] N. Soltani, U. Simon, A. Bahrami, X. Wang, S. Selve, J.D. Epping, M.I. Pech-Canul, M.F.

835 Bekheet, A. Gurlo, Macroporous polymer-derived SiO2/SiOC monoliths freeze-cast from

836 polysiloxane and amorphous silica derived from rice husk, J. Eur. Ceram. Soc. 37 (2017)

837 4809–4820.

838 [67] H. Takagi, K. Maruyama, N. Yoshizawa, Y. Yamada, Y. Sato, XRD analysis of carbon

839 stacking structure in coal during heat treatment, Fuel. 83 (2004) 2427–2433.

840 [68] H.H. El-Maghrabi, S.M. Abdelmaged, A.A. Nada, F. Zahran, S.A. El-Wahab, D. Yahea,

841 G.M. Hussein, M.S. Atrees, Magnetic graphene based nanocomposite for uranium

842 scavenging, J. Hazard. Mater. 322 (2017). doi:10.1016/j.jhazmat.2016.10.007.

843 [69] A. Baylet, P. Marecot, D. Duprez, P. Castellazzi, G. Groppi, P. Forzatti, In situ Raman

844 and in situ XRD analysis of PdO reduction and Pd oxidation supported on γ-Al 2 O 3

845 catalyst under different atmospheres, Phys. Chem. Chem. Phys. 13 (2011) 4607–4613.

846 [70] H. Sun, Y. Zhu, B. Yang, Y. Wang, Y. Wu, J. Du, Template-free fabrication of nitrogen-

847 doped hollow carbon spheres for high-performance supercapacitors based on a scalable

848 homopolymer vesicle, J. Mater. Chem. A. 4 (2016) 12088–12097.

849 [71] J. Wang, V. Schölch, O. Görke, G. Schuck, X. Wang, G. Shao, S. Schorr, M.F. Bekheet,

850 A. Gurlo, Metal-containing ceramic nanocomposites synthesized from metal acetates and

851 polysilazane, Open Ceram. (2020) 100001.

852   [72]   M. Nasr, R. Viter, C. Eid, F. Warmont, R. Habchi, P. Miele, M. Bechelany, Synthesis of

853   novel ZnO/ZnAl 2 O 4 multi co-centric nanotubes and their long-term stability in

854   photocatalytic application, RSC Adv. 6 (2016) 103692–103699.

855   [73]   B.K. Gupta, V. Shanker, M. Arora, D. Haranath, Photoluminescence and electron

856   paramagnetic resonance studies of springlike carbon nanofibers, Appl. Phys. Lett. 95

857   (2009) 73115.

858   [74]   T. Dexin, W. Yanli, G. Ying, Facile Visible-Light-Assisted Synthesis, Optical, and

859   Electrochemical Properties of Pd Nanoparticles with Single-crystalline and Multiple-

860   twinned Structures, Rare Met. Mater. Eng. 46 (2017) 2065–2069.

861   doi:https://doi.org/10.1016/S1875-5372(17)30180-7.

862   [75]   C.-L. Lee, C.-M. Tseng, R.-B. Wu, C.-C. Wu, S.-C. Syu, Catalytic characterization of

863   hollow silver/palladium nanoparticles synthesized by a displacement reaction,

864   Electrochim. Acta. 54 (2009) 5544–5547.

865   doi:https://doi.org/10.1016/j.electacta.2009.04.056.

866   [76]   B.P. Narasaiah, B.K. Mandal, Remediation of azo-dyes based toxicity by agro-waste

867   cotton boll peels mediated palladium nanoparticles, J. Saudi Chem. Soc. 24 (2020) 267–

868   281. doi:https://doi.org/10.1016/j.jscs.2019.11.003.

869   [77]   X. Lu, M. Rycenga, S.E. Skrabalak, B. Wiley, Y. Xia, Chemical Synthesis of Novel

870   Plasmonic Nanoparticles, Annu. Rev. Phys. Chem. 60 (2009) 167–192.

871   doi:10.1146/annurev.physchem.040808.090434.

872   [78]   K.H. Leong, H.Y. Chu, S. Ibrahim, P. Saravanan, Palladium nanoparticles anchored to

873   anatase TiO2 for enhanced surface plasmon resonance-stimulated, visible-light-driven

874 photocatalytic activity, Beilstein J. Nanotechnol. 6 (2015) 428–437.

875 doi:10.3762/bjnano.6.43.

876 [79] J.-H. Kim, A. Mirzaei, H.W. Kim, S.S. Kim, Pd functionalization on ZnO nanowires for

877 enhanced sensitivity and selectivity to hydrogen gas, Sensors Actuators B Chem. 297

878 (2019) 126693.

879 [80] C. Cseko, Z. Bagi, A. Koller, Biphasic effect of hydrogen peroxide on skeletal muscle

880 arteriolar tone via activation of endothelial and smooth muscle signaling pathways, J.

881 Appl. Physiol. 97 (2004) 1130–1137.

882 [81] Y. Zhang, Q. Wang, J. Xu, S. Ma, Synthesis of Pd/ZnO nanocomposites with high

883 photocatalytic performance by a solvothermal method, Appl. Surf. Sci. 258 (2012) 10104–

884 10109.

885 [82] A. Merenda, M. Weber, M. Bechelany, F.-M. Allioux, L. Hyde, L. Kong, L.F. Dumée,

886 Fabrication of Pd-TiO2 nanotube photoactive junctions via Atomic Layer Deposition for

887 persistent pesticide pollutants degradation, Appl. Surf. Sci. 483 (2019) 219–230.

888 [83] T. Chen, S. Yu, X. Fang, H. Huang, L. Li, X. Wang, H. Wang, Enhanced photocatalytic

889 activity of C@ZnO core-shell nanostructures and its photoluminescence property, Appl.

890 Surf. Sci. 389 (2016) 303–310. doi:10.1016/j.apsusc.2016.07.122.

891 [84] Y. Chang, J. Xu, Y. Zhang, S. Ma, L. Xin, L. Zhu, C. Xu, Optical properties and

892 photocatalytic performances of Pd modified ZnO samples, J. Phys. Chem. C. 113 (2009)

893 18761–18767. doi:10.1021/jp9050808.

894 [85] Y.C. Liang, W.K. Liao, X.S. Deng, Synthesis and substantially enhanced gas sensing

895   sensitivity of homogeneously nanoscale Pd- and Au-particle decorated ZnO

896   nanostructures, J. Alloys Compd. 599 (2014) 87–92. doi:10.1016/j.jallcom.2014.01.167.

897   [86] V. Nguyen, J. Si, L. Yan, X. Hou, Electron-hole recombination dynamics in carbon

898   nanodots, Carbon N. Y. 95 (2015) 659–663. doi:10.1016/j.carbon.2015.08.066.

899   [87] V. Nguyen, J. Si, L. Yan, X. Hou, Direct demonstration of photoluminescence originated

900   from surface functional groups in carbon nanodots, Carbon N. Y. 108 (2016) 268–273.

901   doi:10.1016/j.carbon.2016.07.019.

902   [88] P. Erhart, K. Albe, A. Klein, First-principles study of intrinsic point defects in ZnO: Role

903   of band structure, volume relaxation, and finite-size effects, Phys. Rev. B. 73 (2006)

904   205203.

905   [89] I. Iatsunskyi, G. Gottardi, V. Micheli, R. Canteri, E. Coy, M. Bechelany, Atomic layer

906   deposition of palladium coated TiO2/Si nanopillars: ToF-SIMS, AES and XPS

907   characterization study, Appl. Surf. Sci. 542 (2021) 148603.

908   [90] Y. Xie, P.M.A. Sherwood, X-ray photoelectron-spectroscopic studies of carbon fiber

909   surfaces. Part 13. Valence-band studies of oxidized fibers interpreted by X. alpha.

910   calculations, Chem. Mater. 3 (1991) 164–168.

911   [91] A. Barhoum, H.H. El-Maghrabi, A.A. Nada, S. Sayegh, A. Renard, I. Iatsunskyi, E. Coy,

912   M. Bechelany, Simultaneous Hydrogen and Oxygen Evolution Reactions using Free-

913   Standing Nitrogen-Doped-Carbon-Co/CoOx Nanofiber Electrodes Decorated with

914   Palladium Nanoparticles, J. Mater. Chem. A. (2021).

915   [92] J.B. Zhong, J.Z. Li, X.Y. He, J. Zeng, Y. Lu, W. Hu, K. Lin, Improved photocatalytic

916   performance of Pd-doped ZnO, Curr. Appl. Phys. 12 (2012) 998–1001.

917   doi:10.1016/j.cap.2012.01.003.

918   [93] F.S. Hashim, A.F. Alkaim, S.J. Salim, A.H.O. Alkhayatt, Effect of (Ag, Pd) doping on

919   structural, and optical properties of ZnO nanoparticales: As a model of photocatalytic

920   activity for water pollution treatment, Chem. Phys. Lett. 737 (2019) 136828.

921   doi:10.1016/j.cplett.2019.136828.

922   [94] V.M. Daskalaki, I. Fulgione, Z. Frontistis, L. Rizzo, D. Mantzavinos, Solar light-induced

923   photoelectrocatalytic degradation of bisphenol-A on TiO2/ITO film anode and BDD

924   cathode, Catal. Today. 209 (2013) 74–78. doi:10.1016/j.cattod.2012.07.026.

925   [95] Z. Frontistis, V.M. Daskalaki, A. Katsaounis, I. Poulios, D. Mantzavinos, Electrochemical

926   enhancement of solar photocatalysis: Degradation of endocrine disruptor bisphenol-A on

927   Ti/TiO2 films, Water Res. 45 (2011) 2996–3004. doi:10.1016/j.watres.2011.03.030.

928   [96] T.X.H. Le, T. Van Nguyen, Z. Amadou Yacouba, L. Zoungrana, F. Avril, D.L. Nguyen,

929   E. Petit, J. Mendret, V. Bonniol, M. Bechelany, S. Lacour, G. Lesage, M. Cretin,

930   Correlation between degradation pathway and toxicity of acetaminophen and its by-

931   products by using the electro-Fenton process in aqueous media, Chemosphere. 172 (2017)

932   1–9. doi:10.1016/j.chemosphere.2016.12.060.

933   [97] H. Olvera-Vargas, J.C. Rouch, C. Coetsier, M. Cretin, C. Causserand, Dynamic cross-flow

934   electro-Fenton process coupled to anodic oxidation for wastewater treatment: Application

935   to the degradation of acetaminophen, Sep. Purif. Technol. 203 (2018) 143–151.

936   doi:10.1016/j.seppur.2018.03.063.

937   [98] S.O. Ganiyu, N. Oturan, S. Raffy, G. Esposito, E.D. van Hullebusch, M. Cretin, M.A.

938   Oturan, Use of Sub-stoichiometric Titanium Oxide as a Ceramic Electrode in Anodic

939   Oxidation and Electro-Fenton Degradation of the Beta-blocker Propranolol: Degradation

940   Kinetics and Mineralization Pathway, Electrochim. Acta. 242 (2017) 344–354.

941   doi:10.1016/j.electacta.2017.05.047.

942   [99]   M.A. Oturan, M. Pimentel, N. Oturan, I. Sirés, Reaction sequence for the mineralization

943   of the short-chain carboxylic acids usually formed upon cleavage of aromatics during

944   electrochemical Fenton treatment, Electrochim. Acta. 54 (2008) 173–182.

945   doi:10.1016/j.electacta.2008.08.012.

946   [100] P.J. Espinoza-Montero, C. Vega-Verduga, P. Alulema-Pullupaxi, L. Fernández, J.L. Paz,

947   Technologies Employed in the Treatment of Water Contaminated with Glyphosate: A

948   Review, Molecules. 25 (2020) 5550. doi:10.3390/molecules25235550.

949   [101] R. Hernández, I. Olvera-Rodríguez, C. Guzmán, A. Medel, L. Escobar-Alarcón, E. Brillas,

950   I. Sirés, K. Esquivel, Microwave-assisted sol-gel synthesis of an Au-TiO2 photoanode for

951   the advanced oxidation of paracetamol as model pharmaceutical pollutant, Electrochem.

952   Commun. 96 (2018) 42–46. doi:10.1016/j.elecom.2018.09.009.

953   [102] R. Katal, M.H. Davood Abadi Farahani, H. Jiangyong, Degradation of acetaminophen in a

954   photocatalytic (batch and continuous system) and photoelectrocatalytic process by

955   application of faceted-TiO2, Sep. Purif. Technol. 230 (2020) 115859.

956   doi:10.1016/j.seppur.2019.115859.

957   [103] B.O. Orimolade, B.A. Koiki, G.M. Peleyeju, O.A. Arotiba, Visible light driven

958   photoelectrocatalysis on a FTO/BiVO 4 /BiOI anode for water treatment involving

959   emerging pharmaceutical pollutants, Electrochim. Acta. 307 (2019) 285–292.

960   doi:10.1016/j.electacta.2019.03.217.

961   [104] J. Borràs-Ferrís, R. Sánchez-Tovar, E. Blasco-Tamarit, M.J. Muñoz-Portero, R.M.

962   Fernández-Domene, J. García-Antón, TiO 2 nanostructures for photoelectrocatalytic

963   degradation of acetaminophen, Nanomaterials. 9 (2019) 1–13. doi:10.3390/nano9040583.

964